# Geotechnical aspects of offshore wind turbine dynamics from 3D non-linear soil-structure simulations

Kementzetzidis, Evangelos; Corciulo, Simone; Versteijlen, Willem G.; Pisanò, Federico

**DOI**
10.1016/j.soildyn.2019.01.037

**Publication date**
2019

**Document Version**
Accepted author manuscript

**Published in**
Soil Dynamics and Earthquake Engineering

**Citation (APA)**
Kementzetzidis, E., Corciulo, S., Versteijlen, W. G., & Pisanò, F. (2019). Geotechnical aspects of offshore wind turbine dynamics from 3D non-linear soil-structure simulations. *Soil Dynamics and Earthquake Engineering*, *120*, 181-199. https://doi.org/10.1016/j.soildyn.2019.01.037

# Geotechnical aspects of offshore wind turbine dynamics from 3D non-linear soil-structure simulations

**Evangelos Kementzetzidis**
Faculty of Civil Engineering and Geoscience – Geo-Engineering Section
Delft University of Technology
Stevinweg 1, 2628 CN, Delft (The Netherlands)

**Simone Corciulo**
RINA Consulting S.p.A. – Geo & Structures Division
Palazzo R, Via Gran S. Bernardo, 20089, Rozzano (Italy)

**Willem Geert Versteijlen**
Siemens Gamesa Renewable Energy
Prinses Beatrixlaan 800, 2595 BN, Den Haag (The Netherlands)

**Federico Pisanò**
Faculty of Civil Engineering and Geoscience – Geo-Engineering Section / Offshore Engineering Section
Delft University of Technology
Stevinweg 1, 2628 CN, Delft (The Netherlands)
(corresponding author – e-mail: F.Pisano@tudelft.nl)

**Abstract**

The massive development of the offshore wind industry is motivating substantial research efforts worldwide, where offshore wind turbines (OWTs) of increasing size are being installed in deeper water depths. Foundation design is a major factor affecting the structural performance of OWTs, with most installations founded to date on large-diameter monopiles.

This work promotes advanced 3D finite element (FE) modelling for the dynamic analysis of OWT-monopile-soil systems. A detailed FE model of a state-of-the-art 8 MW OWT is analysed by accounting for dynamic soil-monopile interaction in presence of pore pressure effects. For this purpose, the critical-state, bounding surface SANISAND model is adopted to reproduce the hydro-mechanical cyclic response of the sand deposit. The response to realistic environmental loading histories (10 minutes duration) are simulated, then followed by numerical rotor-stop tests for global damping estimation.

While linking to existing literature, all FE results are critically inspected to gain insight relevant to geotechnical design. The modelling tools adopted (i) support the robustness of 'soft-stiff' foundation design with respect to natural frequency shifts, even during severe storm events; (ii) provide values of foundation damping in line with field measurements; (iii) suggest that pore pressure effects may more likely affect soil-monopile interaction under weak-to-moderate environmental loading.

**Keywords**: offshore wind turbine, monopile, cyclic loading, sand plasticity, hydro-mechanical coupling, natural frequency, damping

# 1 Introduction

The high ferment around offshore wind energy fosters massive industrial developments worldwide, especially in Europe and Asia. The case of the booming European market seems particularly meaningful, for instance in light of the 114 new power grids started in the first semester (H1) of 2016 through wind farms in the North, Baltic, and the Irish Sea; significant discussions have been also initiated in southern Europe about the installation of offshore wind turbines (OWTs) in the Mediterranean Sea (Christoforaki and Tsoutsos, 2017; Balog et al., 2016; Schweizer et al., 2016; Zountouridou et al., 2015).

Another distinctive feature of the offshore wind industry is the steady trend towards larger turbine structures and higher power outputs (Figure 1), as witnessed by the frequent press reports about the achievement of new monthly/daily production records – see e.g. 5 MW Gamesa OWT in Spain (2014, monthly record), 8 MW and 9 MW MHI Vestas OWT prototypes in Denmark (daily records in 2014 and 2017, respectively)[1]. The growth in OWT size - increased by 23% in 2017 (5.9 MW on average) with respect to 2016, is being accommodated by improving the installation and performance of foundation systems, primarily large-diameter monopiles. To date, these are still the most widespread foundation concept, adopted for 97%, 100% and 87% of all OWTs installed in Europe in 2015, 2016 and 2017, respectively.

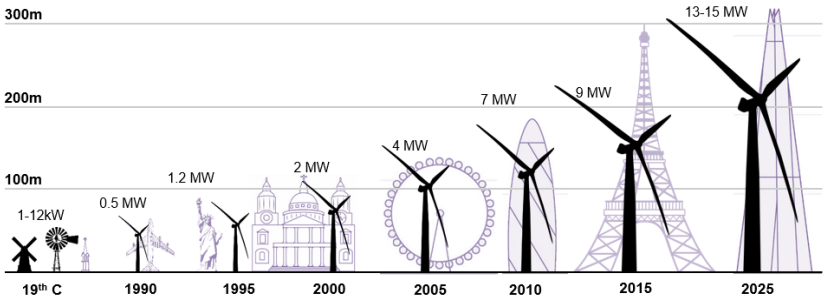


Figure 1: Evolution of wind turbine size and power output (from *Bloomberg New Energy Finance*).

As dynamic-sensitive structures, OWTs and their foundations must be designed with special concern for cyclic/dynamic loading conditions. This is reflected by existing design guidelines (Germanische Lloyd, 2005; DNV, 2014), in which eigenfrequency shifts and intolerable foundation displacements are indicated as possible detriments of the non-linear interaction with the soil. Remarkable research projects have been recently carried out to improve p-y–based design methods for OWT monopiles in light of new large-scale test results (Kallehave et al., 2012; Versteijlen et al., 2017; Byrne et al., 2017). Despite the massive work within the geotechnical community (Pisanò and Gavin, 2017), the operational analysis of monopiles approaching 10 m in diameter is still uncertain in several respects (Doherty and Gavin, 2012; Byrne et al., 2017). Amongst all, certain geotechnical uncertainties are especially relevant to the cyclic/dynamic performance of OWTs (Arany et al., 2017), such as those concerning (i) lateral monopile stiffness and its evolution during strong loading events (storms), (ii) dynamic damping emerging from soil-foundation interaction (Versteijlen et al., 2011), (iii) long-term variations in foundation stiffness and capacity over the whole operational life (Achmus et al., 2009; LeBlanc et al., 2010).

The above foundation issues may all influence the main natural frequency $f_0$ and the global damping of the OWT-monopile-soil system. The first eigenfrequency is a major design driver in so-called 'soft–stiff' approach (Bhattacharya et al., 2013; Kallehave et al., 2015a). The need for reliable $f_0$ estimation has already promoted numerous studies, for instance about the use of

[1]Sources: `www.offshorewind.biz`, `www.mhivestasoffshore.com`

p-y curves (Prendergast and Gavin, 2016; Senanayake et al., 2017) or semi-analytical derivations (Arany et al., 2015, 2016; Shadlou and Bhattacharya, 2016; Versteijlen et al., 2016). Conversely, both conceptual and computational difficulties have hindered so far numerical studies based on 3D non-linear soil-monopile simulations (Cuéllar et al., 2014; Zdravković et al., 2015; Barari et al., 2017; He et al., 2017; Corciulo et al., 2017a,b; Kementzetzidis et al., 2018). In the same arena, accurate assessment of global OWT damping is also extremely relevant to structural/geotechnical design, especially as increasingly large OWTs attain $f_0$ values closer to environmental loading frequencies.

Following the work of Corciulo et al. (2017b), 3D finite element (FE) modelling is further applied to investigate OWT-monopile-sand dynamic interaction, with emphasis on linking structural OWT response to environmental loading and soil non-linearities as predicted via elasto-plastic cyclic modelling – namely, via the critical-state SANISAND04 model by Dafalias and Manzari (2004). Non-linear time-domain simulations are performed to apply advanced geotechnical modelling to the analysis of a last-generation 8 MW OWT under 10 minutes storm histories (considered in industry practice as sufficient duration for 'steady' environmental conditions). Along the line indicated by van Kuik et al. (2016), this work targets new engineering insight into the influence of sand cyclic behaviour on energy dissipation and resonance in OWTs, in a way not possible through simpler, non-3D methods of analysis.

## 2 Integrated OWT–monopile–soil 3D modelling

This section summarises the formulation and set-up of the 3D FE model through the OpenSees simulation platform (`http://opensees.berkeley.edu`; McKenna (1997); Mazzoni et al. (2007)). After a brief summary of the modelling strategy (see also Corciulo et al. (2017b)), the novel aspects of this work are described in more details. These include (i) the adoption of a more advanced critical-state model for cyclic sand behaviour and (ii) its use in 10 minutes dynamic simulations of a large 8 MW OWT-monopile structure.

### 2.1 HM FE modelling of low-frequency soils dynamics

The low-frequency dynamics of the water-saturated soil is described via the $u$–$p$ formulation (Zienkiewicz et al., 1980; Zienkiewicz and Shiomi, 1984), based on the assumption of negligible soil-fluid relative acceleration (López-Querol et al., 2008; Jeremić et al., 2008).

After FE discretisation, spurious checkerboard pore pressure modes in the proximity of the so-called 'undrained-incompressible limit' are avoided by employing the H1-P1ssp stabilised elements proposed by McGann et al. (2015). Their 8-node equal-order formulation exploits a non-residual–based stabilisation (Huang et al., 2004) that produces an additional laplacian term in the pore water mass balance equation, and prevents the simultaneous vanishing of the compressibility and permeability matrices. The stabilisation of pore pressures is controlled by a numerical parameter $\alpha$ to be set as suggested by McGann et al. (2015) – more details about the use/benefits of ssp elements in soil-OWT simulations are available in Corciulo et al. (2017b).

All governing equations are integrated in time through the Newmark algorithm with parameters $\beta = 0.6$ and $\gamma = (\beta + 1/2)^2/4 = 0.3025$ (Hughes, 1987), while explicit forward Euler integration of soil constitutive equations is performed at each stress point (Sloan, 1987).

### 2.2 Critical state plasticity modelling of cyclic sand behaviour

This study relies on the predictive capability of the SANISAND04 model by Dafalias and Manzari (2004), available in OpenSees after the implementation developed at the University of Washington (`http://opensees.berkeley.edu/wiki/index.php/Manzari_Dafalias_Material`; Ghofrani and Arduino (2017)). After the launch of the first SANISAND model (Manzari and Dafalias, 1997),

continual work has been devoted to overcome certain limitations of the original formulation, regarding e.g. dilatancy and fabric effects, hysteretic small-strain behaviour, response to radial stress paths, incremental non-linearity (Papadimitriou et al., 2001; Papadimitriou and Bouckovalas, 2002; Dafalias and Manzari, 2004; Taiebat and Dafalias, 2008; Pisanò and Jeremić, 2014; Dafalias and Taiebat, 2016).

The salient features of the SANISAND04 model adopted herein can be summarised as follows (Dafalias and Manzari, 2004):

- bounding surface formulation including kinematic hardening and Lode-angle dependence;
- adoption of the 'state parameter' concept (Been and Jefferies, 1985; Wood et al., 1994; Manzari and Dafalias, 1997). Accordingly, the model can capture the effects of varying effective confinement and void ratio, and thus simulate the response of a sand in loose to dense conditions with a single set of parameters;
- transition from contractive to dilative response based on the notion of 'phase transformation surface', also termed 'dilatancy surface';
- use of a fabric-related tensor to model phenomenologically fabric changes occurring upon load reversals following stages of dilative deformation. This feature impacts positively the prediction of pore pressure build-up, especially under symmetric/two-way cyclic loading.

The SANISAND framework, however, is not immune from intrinsic limitations, some of which relevant to the problem under consideration. For instance, it should be recalled the known tendency of SANISAND04 to overpredict the pressure build-up rate in medium-dense and dense sand, as well as strain accumulation (ratcheting) under high-cyclic loading. These shortcomings are being considered in recent refinements focused on the modelling of fabric effects (Liu et al., 2018a,b). In conclusion, the FE results presented in the following should be critically regarded in the light of all the above considerations.

**Constitutive parameters** Given the fundamental character of this study, the fifteen parameters in SANISAND04 have not been calibrated for a specific offshore site. Conversely, a homogeneous sand deposit made of Toyoura clean sand is assumed, based on the previous parameter identification performed by Dafalias and Manzari (2004) and reported in Table 1. In the spirit of SANISAND models, a single parameter set can be used to model the behaviour of a given sand at different initial void ratios (or relative density $D_r$) – in the following parametric study the values $D_r$ =40%, 60%, and 80% are considered. The predictive potential of SANISAND04 was originally explored by Dafalias and Manzari (2004) for $D_r <= 64\%$; others authors, such as (Taiebat et al., 2010) and Ramirez et al. (2018), have more recently shown that, despite the above-mentioned limitations, the model is reasonably applicable to denser sands as well (up to $D_r$ =90%).

**Pile-sand interface** The sharp HM discontinuity at the sand-pile interface is treated here by following Griffiths (1985). A thin continuum layer of 'degraded' Toyoura sand is inserted around the monopile, with a thickness equal to 4% the monopile diameter along the shaft, 8% under the tip. The weaker interface sand features elastic shear modulus and critical stress ratio 2/3 and 3/4 times lower than in the intact material, respectively (Table 1). The presence of the thin interface layer aims to partially account for the 'friction fatigue' promoted by initial pile driving (Randolph and Gourvenec, 2011).

## 2.3 OWT and monopile structures

The OWT-monopile set-up assumed in this study is representative of the current industry practice and concerns a large 8 MW OWT founded in medium-dense/dense sand. Relevant structural

Table 1: SANISAND04 parameters for Toyoura sand calibration parameters for (1) the soil domain and (2) the pile-sand interface. Saturated soil mass density: $\rho_{sat} = 1.94\,\mathrm{t/m^3}$, maximum/minimum void ratios (Verdugo and Ishihara, 1996): $e_{max}$= 0.977 and $e_{min}$= 0.597.

| Description | Parameter | Value [ – ] | |
|---|---|---|---|
| | | *Toyoura sand* | *pile-sand interface* |
| Elasticity | $G_0$ | 125 | 83.3 |
| | $\nu$ | 0.3 | 0.3 |
| Critical state | $M$ | 1.25 | 0.938 |
| | $c$ | 0.712 | 0.712 |
| | $\lambda_c$ | 0.019 | 0.019 |
| | $e_0$ | 0.934 | 0.934 |
| | $\xi$ | 0.7 | 0.7 |
| Yielding | $m$ | 0.01 | 0.01 |
| Hardening | $h_0$ | 7.05 | 7.05 |
| | $c_h$ | 0.968 | 0.968 |
| | $n^b$ | 1.1 | 1.1 |
| Dilatancy | $A_0$ | 0.704 | 0.704 |
| | $n^d$ | 3.5 | 3.5 |
| Fabric | $z_{max}$ | 4 | 4 |
| | $c_z$ | 600 | 600 |

details – confidential courtesy of Siemens Gamesa Renewable Energy (The Hague, Netherlands) – have been all incorporated in the numerical model. In particular, Figure 2a illustrates on the left-side the prototype OWT considered, featuring (i) a monopile with diameter $D = 8$ m, underground length $L_{pile} = 27$ m and average thickness $t = 62$ mm, (ii) a superstructure with mudline-to-hub distance of approximately 150 m, and (iii) a rotor with blade length $L_{blade}$ in the order of 75 m. The OWT model also includes structural and equipment masses (flanges, transition piece, boat landing, and working platforms, etc.), as well as the lumped mass and rotational inertia of the RNA (Rotor-Nacelle Assembly). Added mass effects due to the surrounding seawater are introduced in the simplified form of nodal lumped masses evenly distributed along the water depth – here $H_w = 26$ m – and calculated as twice the water mass in the submerged OWT volume (Newman, 1977; Corciulo et al., 2017b).

The steel structure above the mudline (wind tower and part of the monopile) is modelled as an elastic beam with variable cross-section and subdivided into approximately 160 Timoshenko beam elements with consistent (non-diagonal) mass matrix. The underground portion of the tubular monopile is instead modelled as a 3D hollow cylinder, discretised by using 8-node, one-phase ssp bricks $(H1ssp)$[2] (Figure 2b).

A major issue in the dynamic simulation of OWTs concerns the modelling of all sources of energy dissipation (damping). In particular:

– most energy dissipation takes place within the soil domain as plastic/hysteretic damping and wave radiation away from the monopile. Wave radiation, often insignificant in the low-frequency range, is allowed through absorbing viscous dampers set along the lateral domain boundaries (Corciulo et al., 2017b);

– structural damping is introduced based on the Eurocode 1 (BS EN, 1991). A (Rayleigh) damping ratio $\zeta_{steel} = 0.19\%$ is assigned to all steel cross-sections at the pivot frequencies 0.1 and 80 Hz;

[2]The satisfactory bending performance of 3D ssp monopiles is documented in Corciulo (2016).

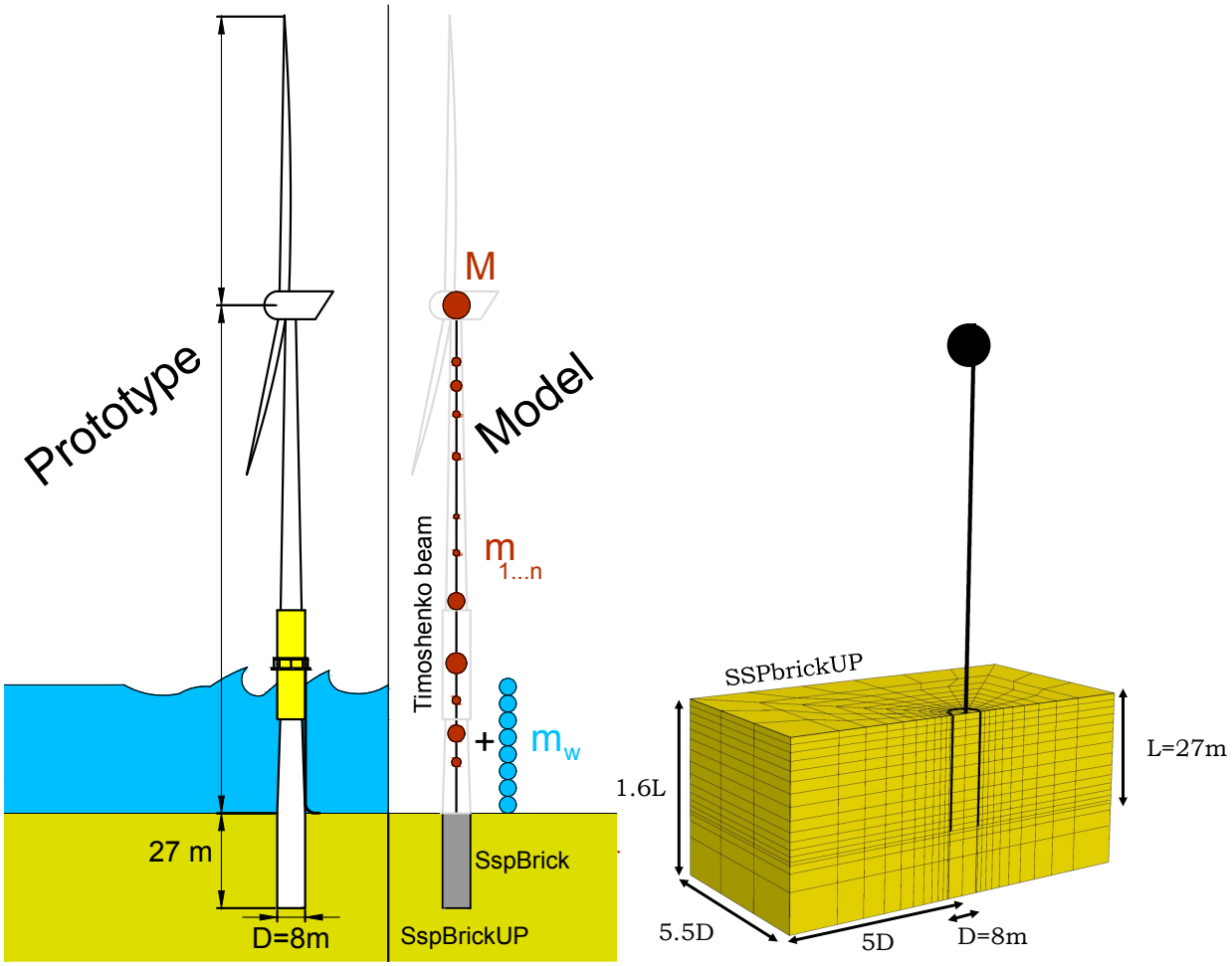


(a) OWT size and mass distribution

(b) size and FE mesh of the soil domain

Figure 2: Idealisation and FE modelling of the OWT-foundation-soil system.

– hydrodynamic damping is incorporated following (Leblanc and Tarp-Johansen, 2010), where a damping ratio of 0.12% due to wave radiation is obtained for an OWT with $f_0 = 0.3$ Hz, pile diameter of 4.7 m and water depth at 20 m. In the lack of more specific data, a damping ratio of $\zeta_w = 0.12\%$ is assigned to the added water mass nodes;

– aerodynamic damping is not part of the total damping identified later in this study, although it is implicitly included in the wind loading histories applied to the OWT.

It should be noted that the monopile size in Figure 2a was designed at Siemens Gamesa Renewable Energy for specific/confidential sandy soil conditions. To set at least "likely" soil conditions, approximate equivalence was sought between the original inhomogeneous site and an ideal homogeneous 'Toyoura sand site' with initial relative density $D_r$ = 70-80% and SANISAND04 parameters in Table 1. In particular, good consistency was also observed between the peak frictional angles resulting from SANISAND04 simulations and available cone resistance data – the latter were originally employed to calibrate relevant p-y curves for monopile design. As for cyclic behaviour, Toyoura sand parameters had to be assumed as a reference, due to the lack of specific laboratory data.

## 2.4 Space/time discretisation

Under the simplifying assumption of mono-directional lateral loading, only half OWT is modelled for computational convenience. The accuracy and efficiency of FE results depend strongly on space/time discretisation, an aspect that received considerable attention at the beginning of this work – as documented in Kementzetzidis (2017). Apart from their suitable undrained-incompressible performance, the 8-noded H1-P1ssp elements devised by McGann et al. (2015) remedy undesired locking effects without very fine meshing, owing to their enhanced assumed strain field formulation. The final domain size and ssp element distribution are as shown in Figure 2b, and reproduce quite closely the discretisation choices more widely discussed in Corciulo et al. (2017b). As for time marching, suitable step size $\Delta t$ had to be tuned case-by-case depending on the loading amplitude, soil relative density, and permeability, etc.

## 2.5 Loading scenarios and parametric studies

The OWT-monopile-soil dynamic response is discussed in the following with reference to different 10 minutes loading scenarios:

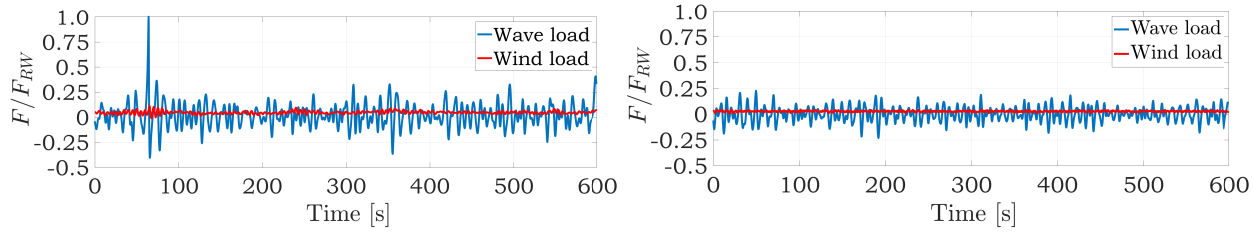


Figure 3: Loading scenarios (courtesy of Siemens Gamesa Renewable Energy): (a) Case A – storm with rogue wave (50 years return period); (b) Case B – strong storm. Force amplitudes normalised with respect to $F_{RW}$, (confidential) load amplitude of the rogue wave thrust in case A.

- Case A, representative of a storm with 50-years return period, involving an average wind speed of 47 m/s and an approximately 10 m-tall rogue wave hitting the OWT after about 70 s (Figure 3a). The OWT is assumed in idling state with blades pitched out (feathering);
- Case B, different heavy storm loading arising from a 24 m/s average wind speed (Figure 3b). The OWT is assumed in production with blades significantly (but not entirely) pitched out;
- Case C, weak load scenario obtained by rescaling the load amplitudes in Case B by a factor of 5 (not plotted in Figure 3 for brevity).

Both cases A and B are dominated by two-way/cyclic wave loading (Figure 3). Case C has been simplistically obtained to compare OWT responses associated with high (the focus of this work) and low soil non-linearity under same input frequency content.

The total wave force is distributed along the submerged OWT nodes, accounting for the actual wave height – nodes up to 10 m above the mean sea level are loaded during wave impact to ensure realistic simulation. As the OWT blades would be completely (Case A) or significantly (Case B) pitched out under such storms, preliminary load simulations performed at Siemens Gamesa returned wind drag forces along the hub and the tower at negligible aerodynamic damping.

All FE analyses are run beyond ten minutes to reproduce so-called 'rotor-stop' tests, with the purpose of investigating global soil damping via the well-known logarithmic decrement approach. Rotor-stops are simulated here by switching off all lateral loads at $t = 600$ s and letting the OWT to vibrate freely for approximately ten periods.

Table 2: FE analysis programme – list of considered (i) loading scenarios, sand (ii) relative density ($D_r$) and (iii) permeability ($k$).

| $D_r$ | | 80% | 60% | 40% |
|---|---|---|---|---|
| Loading scenario | Case A | $k = 10^{-5}$ m/s | $k = 10^{-4,-5,-6}$ m/s | $k = 10^{-5}$ m/s |
| | Case B | $k = 10^{-5}$ m/s | $k = 10^{-4,-5,-6}$ m/s | $k = 10^{-5}$ m/s |
| | Case C | $k = 10^{-5}$ m/s | $k = 10^{-4,-5,-6}$ m/s | $k = 10^{-5}$ m/s |

**Analysis programme** The whole analysis programme (15 in total) is detailed in Table 2 and relates to the following observations:

- heuristically, the (confidential) site conditions that generated the monopile design in Figure 2a may be classified as sandy soil with $D_r$ =70-80%. For this reasons, the OWT response to the load cases A, B and C is simulated for both $D_r = 60\%$ and $D_r = 80\%$, with the latter most likely more representative of the real site;
- the case $D_r = 40\%$ is also considered in the parametric study. Although unrealistic, such a case is useful to detect very extreme effects of soil non-linearity, and to warn about the detriments of poor geotechnical design;
- only for the intermediate $D_r = 60\%$, the effect of soil permeability is explored over three orders of magnitudes ($k = 10^{-4,5,6}$ m/s), relevant to poorly graded sands, gravelly sands with low fine content.

# 3 Dynamic sand-monopile interaction

In this section, the non-linear performance of the FE model is inspected and discussed to highlight relevant aspects of dynamic sand-monopile interaction.

## 3.1 Sand HM response and void ratio effects

The HM sand response to the strongest loading case (Case A) is illustrated in the following for the six control points ($A_{L,R}$, $B_{L,R}$, $C_{L,R}$) indicated in Figure 4. The results in the following relate to a single permeability ($k = 10^{-5}$ m/s) and three different initial void ratios ($D_r = 40$, 60, 80%).

**Pore water pressure** The pore pressure $u$ in the soil domain evolves during pile vibration depending on (i) changes in mean stress $p$, (ii) plastic volume contraction/expansion under shear loading and (iii) drainage conditions. Figure 5 depicts the time evolution of the $u/p$ ratio at the abovementioned control points, for Case A only. At all points considered pore pressure build-up is observed, more pronouncedly for the loosest sand and with temporary peaks of negative excess pore pressure that are instead higher for the densest (most dilative) sand. The liquefaction limit $u/p = 1$ is never attained in the $D_r = 80\%$ (most relevant to the monopile design under consideration). The effect of the rogue wave stands out after approximately 70 seconds in the form of an abrupt decrease of the pore pressure ratio (and of the absolute pressure as well) for all $D_r$ and at all control points.

To provide a wider picture of the excess pore pressure field $\Delta u$ in case A, $\Delta u$ contour plots at $t = 300$ s are shown in Figure 6 for all $D_r$ values, with apparent influence of $D_r$ on the hydraulic response of the sand deposit. In the relevant case of dense sand, the highest excess pore pressures

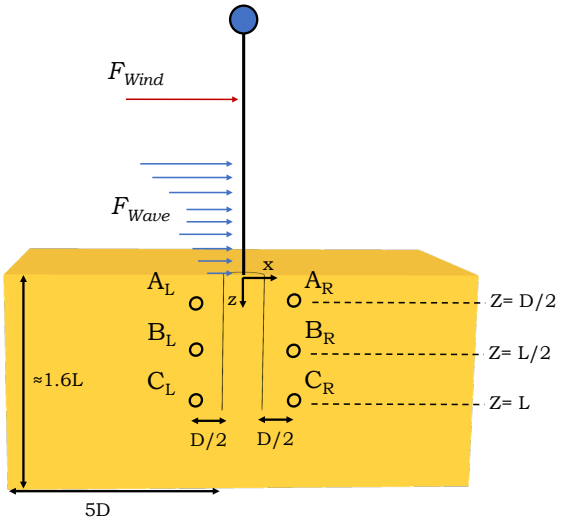


Figure 4: OWT model and location of the control points $A_{L,R}$, $B_{L,R}$, $C_{L,R}$ within the soil domain.

occur at the pile tip, whereas a more uniform spread of $\Delta u$ (and lower values) can be observed at lower $D_r$. As weaker sands are considered, wider plastic stress redistribution takes place within the domain, with a direct effect on the plastic strain and pore water pressure fields.

The results in Figure 5 concern soil locations closely around the monopile, hence the significant pore pressures predicted. However, (partial) sand liquefaction does not affect here the whole soil deposit (Figure 6), as it could do under seismic loading conditions. Therefore, the stiffness/strength of further soil locations are not fully compromised, with positive impact on the OWT performance – see results in Section 5.

**Stress paths and shear stress-strain response** The soil response to the loading case A is illustrated in Figures 7–8 in terms of effective stress paths ($\tau_{xz} - p'$) and shear stress-strain response ($\tau_{xz} - \gamma_{xz}$) for $D_r = 80\%$. The same plots for $D_r = 40\%$ are reported in Figure 9 – though only for points $B_{L,R}$.

High soil non-linearity can be clearly noticed in all cases as the OWT is impacted by the rogue wave, especially at the shallowest control points (with low $p'$) and for the lowest $D_r$. In particular, the sand with $D_r = 40\%$ relative density develops more than double shear straining than in the case with $D_r = 80\%$ at all control points. That is the result of the loss in soil stiffness induced by pore pressure build-up. Although the $D_r = 40\%$ is not representative of original design conditions, the potential risks of HM non-linearity should be acknowledged and related to the chance of excessive deflections/rotations at the pile head.

## 3.2 Monopile head response

Simulated lateral pile head displacements are plotted in Figure 10 for cases A, B, C and all $D_r$ considered. The final 60 s in all plots concern the final rotor-stop phase and will be discussed in the following section.

As expected, pile head displacements are much higher under strong loading (cases A and B) than for the weak event C, while the effect of the initial void ratio is also visible through the differences in displacement accumulation from $D_r = 80\%$ to $D_r = 40\%$.

It is worth reminding, however, that SANISAND models are not accurate in simulating soil ratcheting, and therefore the displacement trends in Figure 10 might be of mainly qualitative value.

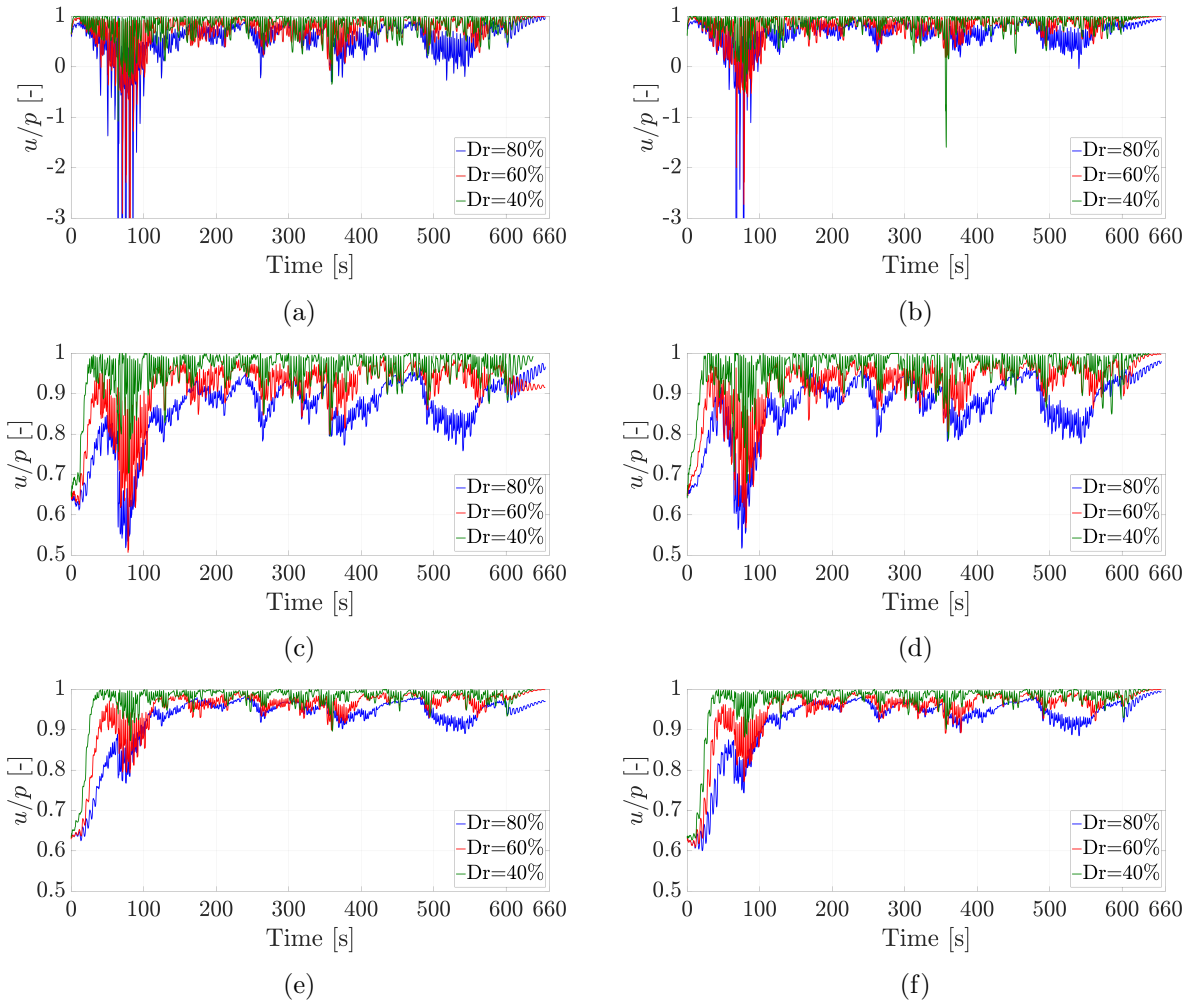


Figure 5: Time evolution of the pore pressure ratio $u/p$ at the control points in Figure 4, *CaseA*: (a) $A_L$, (b) $A_R$, (c) $B_L$, (d) $B_R$, (e) $C_L$, (f) $C_R$.

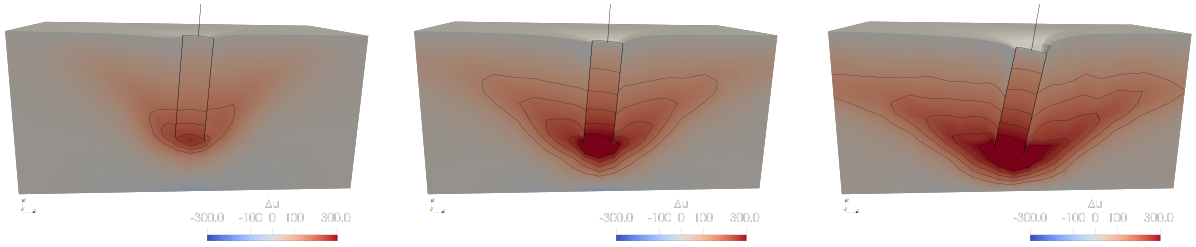

$DR = 80\%$ $DR = 60\%$ $300s: \ DR = 40\%$

Figure 6: Excess pore pressure contour plots at 300 s of Case B for $D_r$ = 80%, 60% and 40%. Colorbars indicate $\Delta u$ in the range [-300 kPa; 300 kPa].

Substantial improvements in this area are expected soon through a new SANISAND formulation with ratcheting control (Liu et al., 2018a).

The monopile response affects OWT dynamics through the rotational and lateral stiffnesses evaluated at the pile head. Moment-rotation plots for Case A and Case B are illustrated in Figure 11 for $D_r$ = 80%, 60%, 40%; the two dashed lines in each subfigure highlight the evolution of the secant rotational stiffness from the beginning to the end of the simulation. The decrease in rotational stiffness is obvious as soil plastifications develop, and seems quite catastrophic for the

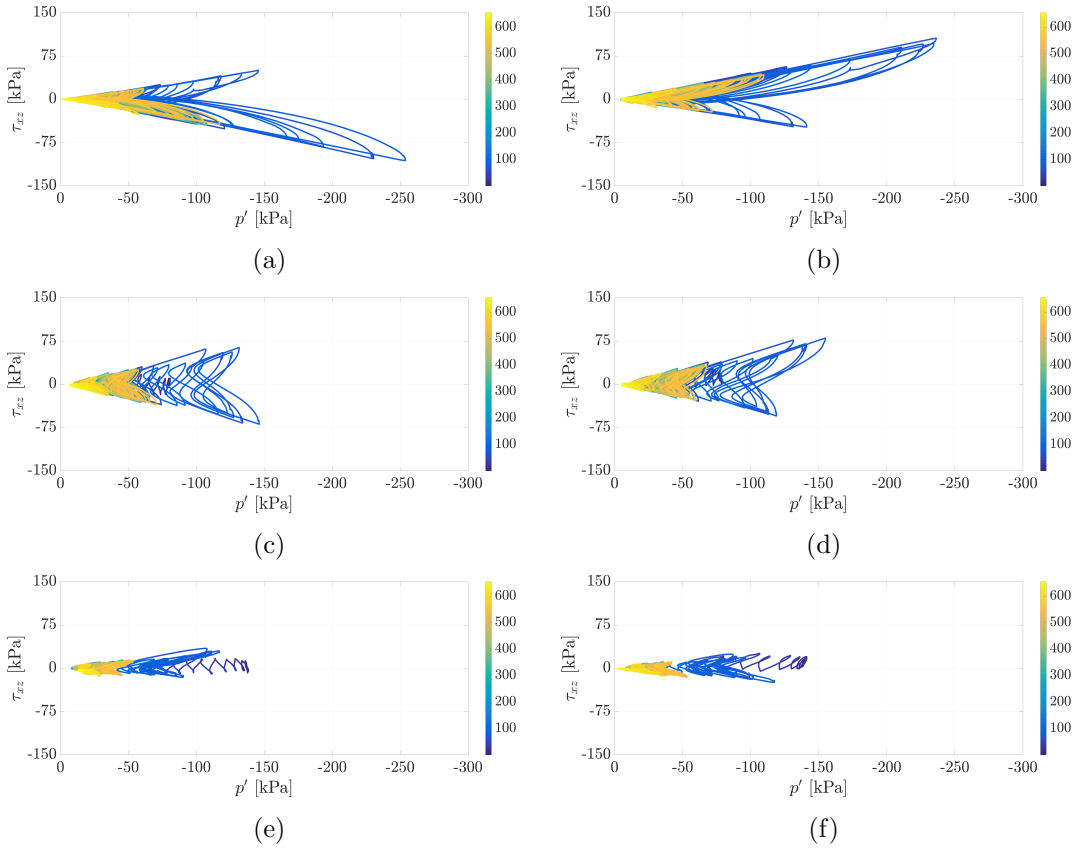


Figure 7: Stress paths $\tau_{xz} - p'$ at all control points, $D_r = 80\%$, Case A: (a) $A_L$, (b) $A_R$, (c) $B_L$, (d) $B_R$, (e) $C_L$, (f) $C_R$. The colours in the sidebars indicate time in seconds.

virtual misdesign associated with $D_r = 40\%$ (see Table 3).

Table 3: Rounded lateral and rotational pile head stiffnesses at the beginning of the analysis ($K_{L,0}$, $K_{R,0}$) and at approximately 600 s ($K_L$, $K_R$) for Cases A and B, and $D_r = 80\%$, 60%, 40%.

| | | $D_r$ | | |
|---|---|---|---|---|
| | Stiffness | 80% | 60% | 40% |
| Case A | $K_{L,0}$ [MNm$^{-1}$] | 115 | 64 | 45 |
| | $K_{R,0}$ [GNmrad$^{-1}$] | 99 | 74 | 60 |
| | $K_L$ [MNm$^{-1}$] | 95 | 45 | 36 |
| | $K_R$ [GNmrad$^{-1}$] | 79 | 48 | 34 |
| Case B | $K_{L,0}$ [MNm$^{-1}$] | 168 | 139 | 85 |
| | $K_{R,0}$ [GNmrad$^{-1}$] | 100 | 84 | 67 |
| | $K_L$ [MNm$^{-1}$] | 94 | 47 | 26 |
| | $K_R$ [GNmrad$^{-1}$] | 60 | 51 | 26 |

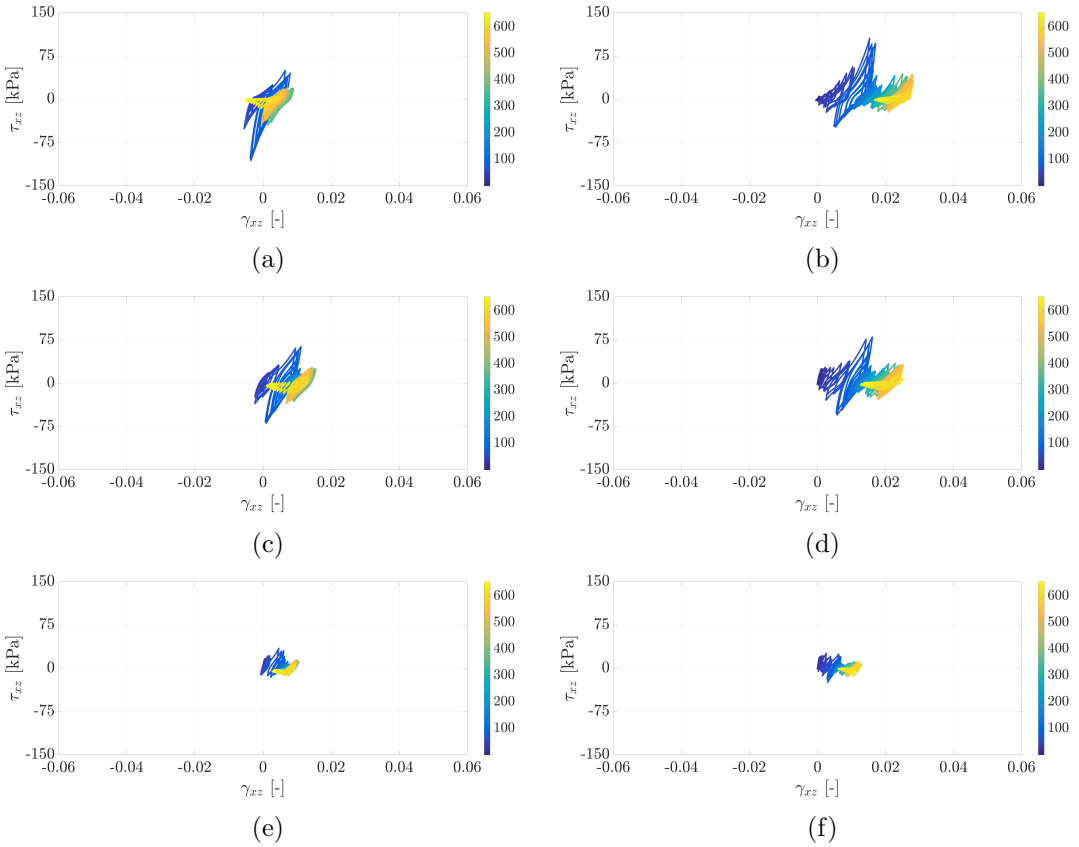


Figure 8: Shear stress-strain responses $\tau_{xz} - \gamma_{xz}$ at all control points, $D_r = 80\%$, Case A: (a) $A_L$, (b) $A_R$, (c) $B_L$, (d) $B_R$, (e) $C_L$, (f) $C_R$. The colours in the sidebars indicate time in seconds.

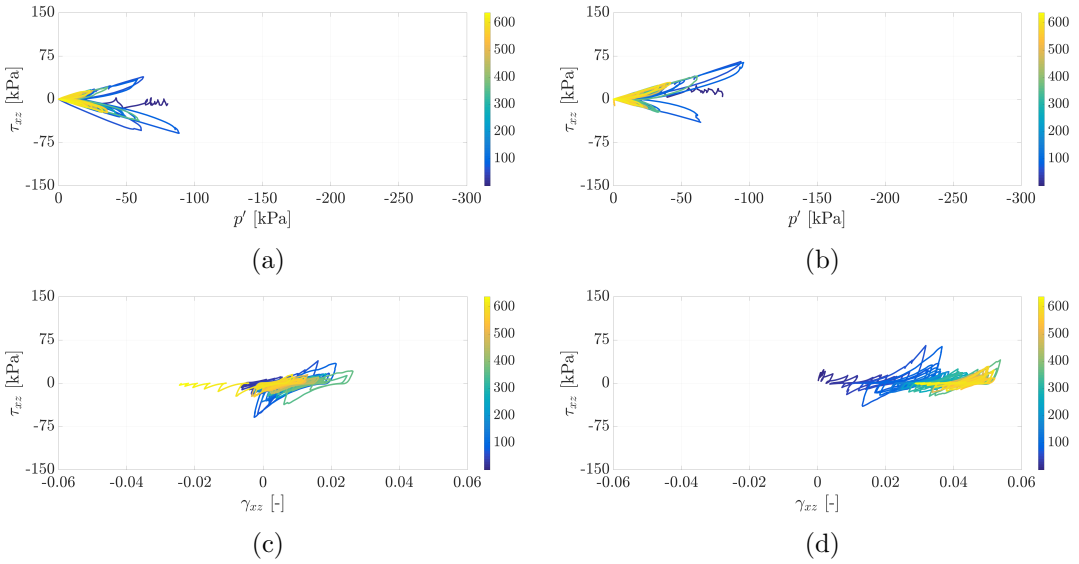


Figure 9: Stress paths and shear stress-strain responses at control points $B_{L,R}$, $D_r = 40\%$, Case A: $\tau_{xz} - p'$ – (a) $B_L$, (b) $B_R$; $\tau_{xz} - \gamma_{xz}$ – (c) $B_L$, (d) $B_R$. The colours in the sidebars indicate time in seconds.

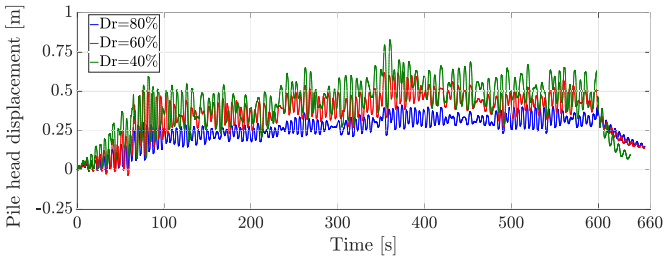


(a) Case A

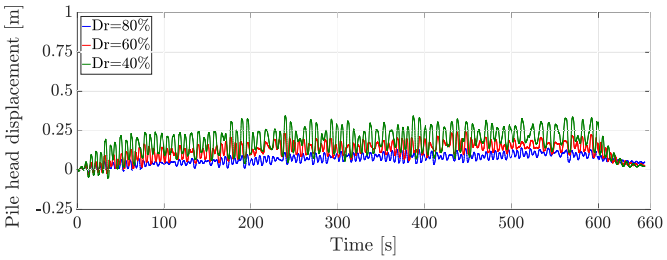


(b) Case B

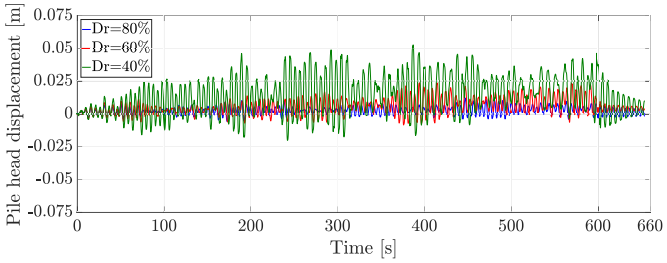


(c) Case C

Figure 10: Lateral displacement of the monopile head (note the different vertical axis scale in Case C).

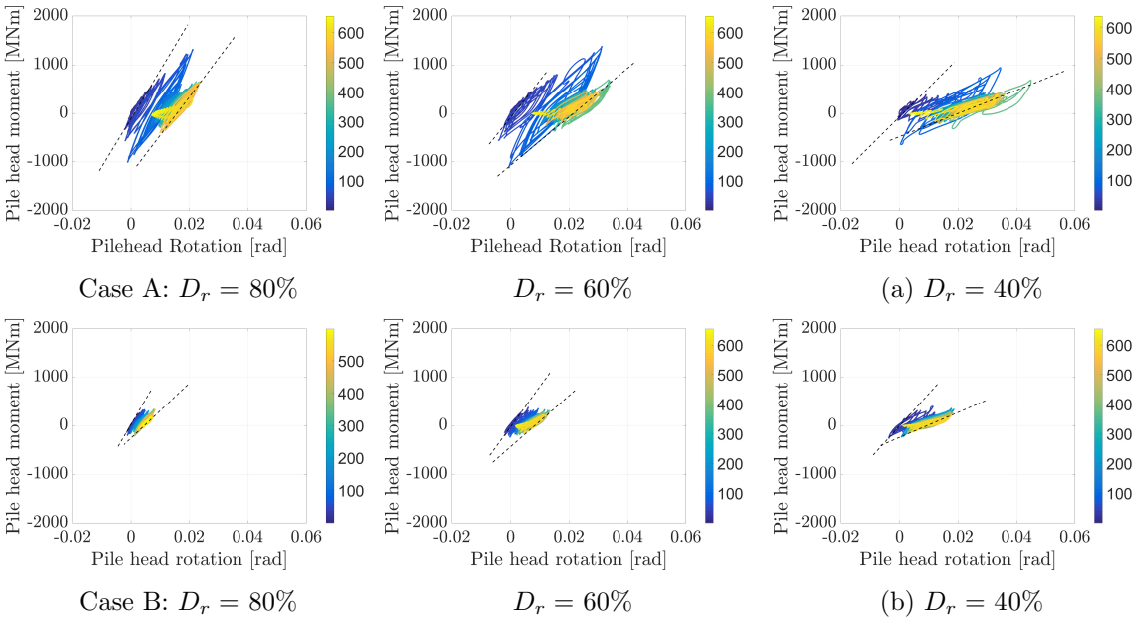


Figure 11: Moment-rotation response at the pile head for cases A and B. The colours in the sidebars indicate time in seconds, whereas dashed lines point out the variation of the rotational stiffness $K_R$.

# 4 OWT damping

Total dynamic damping $\zeta$ is very relevant to OWT design, for instance in relation to fatigue damage. However, substantial uncertainties still affect its estimation, especially about the component of $\zeta$ arising from soil-foundation interaction (Germanische Lloyd, 2005; Versteijlen et al., 2011). A number of studies have been carried out to fill this gap, in most cases by performing emergency OWT shut-downs, i.e. rotor-stop tests (Tarp-Johansen et al., 2009; Versteijlen et al., 2011; Damgaard et al., 2012, 2013; Shirzadeh et al., 2013; Carswell et al., 2014). Table 4 provides a synopsis of methodologies and inferences from the cited literature studies, as well as a solid ground to assess this study's results – extracted from the most meaningful cases $D_r$ = 60-80%. Table 4 enables to distinguish different sources of dissipation based on the following simplification:

$$\zeta_{total} = \zeta_{struct} + \zeta_{foundation} \tag{1}$$

where the total damping ratio $\zeta_{total}$ results from the sum of $\zeta_{struct}$ (viscous Rayleigh damping within the steel OWT tower) and $\zeta_{foundation}$ (from plastic straining and wave radiation within the soil) – aerodynamic damping is neglected. The simplistic split in Equation (1) is usually deemed appropriate in the low damping regime. The component $\zeta_{foundation}$ is directly affected by soil energy dissipation as locally simulated by the SANISAND04 model. The predicted damping behaviour of Toyoura sand is discussed in Dafalias and Taiebat (2016) in comparison to a recent hypoplastic version of the same model. As usual in standard bounding surface plasticity, the resulting damping ratio of the sand is somewhat overpredicted for shear strain levels beyond 1%, so that the $\zeta_{foundation}$ values simulated for harsh environmental conditions should be regarded as upper bounds.

Table 4: Literature review of total damping ratios for monopile-supported OWTs (table adapted after Carswell et al. (2014)). For the present study, the most realistic results obtained for $D_r$ = 60-80% are reported.

| | Tarp-Johansen et al. (2009) | Versteijlen et al. (2011) | Damgaard et al. (2012) | Damgaard et al. (2013) |
|---|---|---|---|---|
| Method | experimental | experimental | experimental | experimental |
| Analysis | 3D FEM | modified p-y | hysteretic p-y | hysteretic p-y |
| Turbine | 3.5 MW (Scaled NREL 5 MW) | Siemens 3.6 MW | - | Vestas |
| Soil | sandy or clayey from the North Sea | medium dense sand and clay | top layer loose sand,very stiff to very hard clay | medium-dense sand and soft clay |
| Monopile (L/D) | 4.26 | 4.68 | 5.38 | - |
| Wind velocity | - | 11-19.7 m/s | 3-13 m/s | - |
| $\zeta_{foundation}$ | 0.56%-0.80% | 1.5% | 0.58% | 0.8%-1.3% |
| $\zeta_{struct}$ | 0.19% | 1.5% | 0.19% | - |
| $\zeta_{total}$ | 0.75%-0.99% | 3% | 0.77% | 0.8%-1.3% |

| | Shirzadeh et al. (2013) | Carswell et al. (2014) | This study ($D_r$ = 60-80%) | |
|---|---|---|---|---|
| Method | experimental | numerical | numerical | |
| Analysis | HAWC2, Rayleigh | 2D and 3D FE | 3D FE | |
| Turbine | Vestas | NREL 5 MW | Siemens 8 MW | |
| Soil | dense sand with layer of stiff clay | soft, stiff and hard clay | Medium dense and dense sand | |
| Monopile (L/D) | 4.12 | 5.67 | 3.38 | 3.38 |
| Wind velocity | 4.5-6.5 m/s | - | low | 24-47 m/s |
| $\zeta_{foundation}$ | 0.25% | 0.17%-0.28% | 0.56%-2.1% | 2%-5.7% |
| $\zeta_{struct}$ | 0.6% | 1.00% | 0.19% | 0.19% |
| $\zeta_{total}$ | 0.85% | 1.17%-1.28% | 0.76%-2.3% | 2.2%-5.9% |

It should also be noted that previous rotor-stop experiments have been all executed under low wind conditions – except for the case of Versteijlen et al. (2011), regarding OWT either in production or feathered. There is no information available about soil damping during heavy storms, as in fact, no rotor-stopping is possible for parked turbines (i.e. beyond the cut-off wind speed). Conversely, after-storm rotor-stops can well be simulated numerically, as done in this

Table 5: Total OWT damping ratios for all analysis cases.

| *Relative density* $D_r$ | | 80% | 60% | | | 40% |
|---|---|---|---|---|---|---|
| *Permeability* $k$ | | $10^{-5}$ m/s | $10^{-4}$ m/s | $10^{-5}$ m/s | $10^{-6}$ m/s | $10^{-5}$ m/s |
| *Loading* | Case A-B | $\zeta \approx 2.2\%$ | $\zeta \approx 5.4\%$ | $\zeta \approx 5.15\%$ | $\zeta \approx 5.9\%$ | $\zeta \approx 7.7\%$ |
| *Scenario* | Case C | $\zeta \approx 0.76\%$ | $\zeta \approx 0.79\%$ | $\zeta \approx 1.3\%$ | $\zeta \approx 2.3\%$ | $\zeta \approx 2.9\%$ |

study by suddenly unloading the OWT after 10 minutes of forced vibration. Global damping values have been obtained via the well-known logarithmic decrement method, applied here to the lateral acceleration histories of the OWT hub after low-pass filtering below 0.35 Hz (Figure 12)[3].

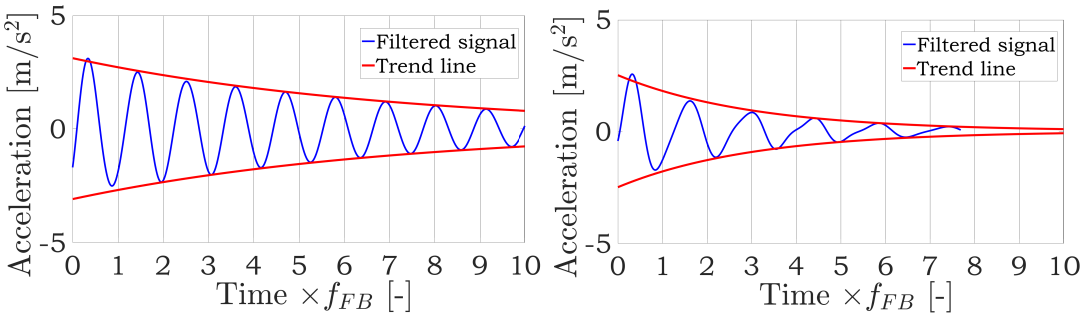


(a) $D_r = 80\%$ (b) $D_r = 40\%$

Figure 12: Estimation of global OWT damping ratios from time histories of OWT hub acceleration after rotor-stopping (Case A). Time is normalised with respect to the fixed-based natural frequency of the OWT ($f_{FB}$).

Table 5 summarises the set of simulated damping values, all in substantial agreement with the trends from previous literature – compare to Table 4. The OWT damping after Case A and Case B loading are in all cases very similar, thus listed together in Table 5.

## 4.1 Influence of load amplitude

The amplitude of forced vibrations prior to rotor-stop affects apparently the entries of Table 5, with damping values for cases A-B higher than for the fictitious weak-loading Case C.

The overview in Table 4 also allows relating the load dependence of OWT damping to previous studies. Taking wind speed as a measure of load severity, it is not surprising to find that cases A-B in this study (wind speed >24 m/s) result in the highest damping values, followed in order by the results of Versteijlen et al. (2011), Damgaard et al. (2012) and Shirzadeh et al. (2013). Lower wind speeds correlate in all cases with lower damping, even in the purely numerical Case C[4].

As energy dissipation through wave radiation (geometrical spreading) is deemed negligible for frequencies lower than 1 Hz (Tarp-Johansen et al., 2009; Damgaard et al., 2013), it should be concluded that most foundation damping arises from soil plasticity. Pore pressures influence the global OWT damping only through a direct effect on the effective stresses within the soil

[3]Global damping ratio values have been obtained based on the whole free oscillation history of the OWT hub. This involved approximately ten periods in all cases, although with much more marked amplitude decays for $D_r$= 40%.

[4]The hub acceleration simulated for Case C at load removal is in the range of those recorded by Devriendt et al. (2013); Damgaard et al. (2012, 2013) for low wind speeds in the order of $\approx 3 - 13$ m/s).

and, in turn, on its (mechanical) non-linear response. Indeed, the adopted $u-p$ formulation relies on the common assumption of 'strong viscous coupling' (Gajo, 1995; Schanz, 2009), with no velocity-proportional dissipation resulting from grain-water drag interaction (Jeremić et al., 2008) – usually more relevant at higher frequencies.

## 4.2 Influence of sand permeability

The 3D numerical study of Corciulo et al. (2017b) concluded that sand permeability does not affect significantly the dynamics of OWTs, but only certain features of the local foundation response. That conclusion, made for strong loading scenarios, is confirmed here by the damping ratios in Table 5 associated with cases A-B, almost insensitive to permeability values varying over three orders of magnitude ($D_r = 60\%$). In contrast, the $k$-dependence of $\zeta$ seems much more pronounced in Case C, even though pore pressure effects are usually associated with soil non-linearity.

Figure 13 helps explaining this counter-intuitive finding, supported by the use of a soil model in which volume changes can impact both stiffness and strength properties. Figures 13(a)-(c) display substantial differences in the excess pore pressure field at varying permeability, with expected highest $\Delta u$ for $k = 10^{-6}$ m/s. Relatedly, Figure 13d shows for the control point $A_R$ (Figure 4) that partial drainage and soil densification occur for $k = 10^{-4}$ m/s, whereas similar undrained conditions characterise $k = 10^{-5,-6}$ m/s. These differences in HM response cause different displacement time histories at the monopile head, as readily apparent in Figure 13e. Such a sensitivity to permeability may not emerge under very strong loading: in that case, the soil volume changes induced by shear loading are likely to reach their non-linear upper limit for any realistic permeability, so as to establish nearly undrained conditions regardless (Corciulo et al., 2017b).

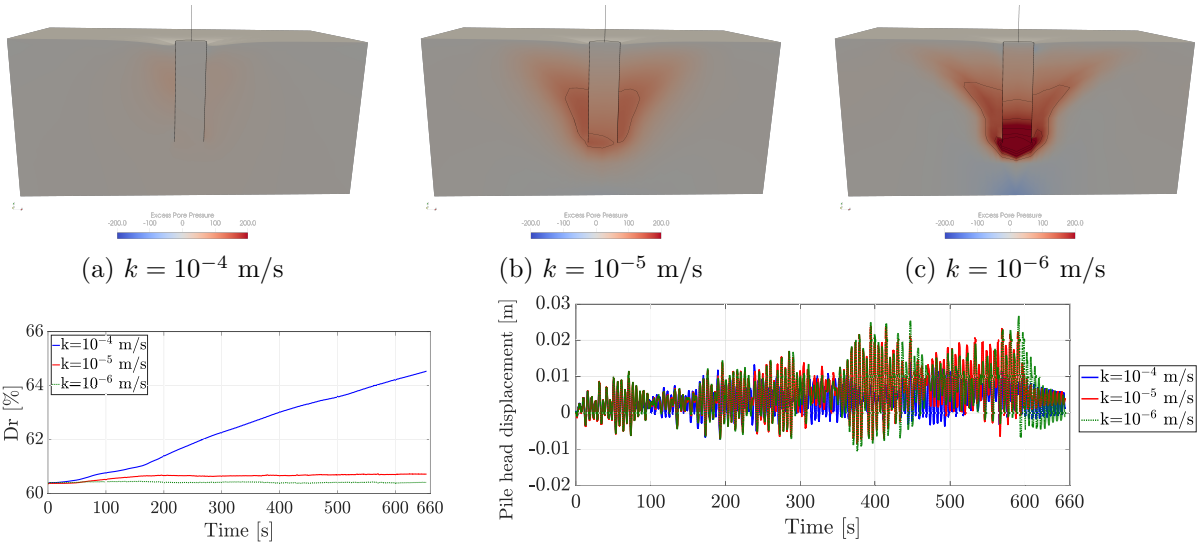


(a) $k = 10^{-4}$ m/s (b) $k = 10^{-5}$ m/s (c) $k = 10^{-6}$ m/s

(d) $D_r$ at $A_R$ (e) pile head displacement

Figure 13: Influence of permeability on the soil response in Case C–$D_r = 60\%$: (a-c) $\Delta u$ contour plots at $t = 600$ s; (d) $D_r$ evolution at control point $A_R$; (e) lateral displacement of the monopile head.

# 5 OWT natural frequency

In this section, the frequency response of the OWT-monopile-sand system is discussed. Emphasis is on predicting the natural frequency $f_0$ of the turbine, and its evolution in time in relation to

Table 6: $f_0/f_{FB}$ values estimated as per Arany et al. (2017) with different formulations of foundation stiffness.

| $D_r$ | 80% | 60% | 40% | Soil-pile interaction model |
|---|---|---|---|---|
| $E_{0,z=Dp}$ | 71.3 MPa | 63.4MPa | 56.9 MPa | |
| | 0.899 | 0.895 | 0.890 | Randolph (1981) – flexible |
| | 0.913 | 0.908 | 0.904 | Gazetas (1984) – flexible |
| $f_0/f_{FB}$ | 0.881 | 0.872 | 0.867 | Shadlou and Bhattacharya (2016) – flexible |
| | 0.977 | 0.963 | 0.954 | Shadlou and Bhattacharya (2016) – rigid |

geotechnical/loading conditions.

## 5.1 Natural frequency from analytical modelling

As a first step, $f_0$ is evaluated according to the analytical approach reported by Arany et al. (2017) and based on Arany et al. (2015). The main calculation steps are summarised in Appendix A.1 and focus on the contribution of the foundation compliance to the global OWT dynamics.

Table 6 reports the $f_0$ values obtained for all $D_r$ from 80% to 40% and normalised with respect to the fixed-base natural frequency $f_{FB}$ – loading inputs are irrelevant to linear elastic calculations. The table points out quantitative differences arising from different formulations of the lateral/rotational foundation stiffness (Randolph, 1981; Shadlou and Bhattacharya, 2016; Gazetas, 1984). The relative density of the soil affects $f_0$ through the representative small-strain stiffness $E_{0,z=D_p}$ (see Appendix A.1), but with no chance of capturing non-linear HM effects.

## 5.2 Frequency response from 3D FE simulations

The FE results in terms of OWT hub displacement are inspected for all cases in Table 2 and sand permeability $k = 10^{-5}$ m/s.

### 5.2.1 Response power spectra

A first grasp of simulated OWT frequency responses can be attained through Figure 14, in which hub displacement power spectra normalised with respect to the maximum peak ($PSD_{norm}$) are illustrated and compared to the corresponding spectra of total lateral load histories (from Figure 3). Plotted for all cases are also the analytical $f_0/f_{FB}$ values associated OWT on fixed (green lines) and compliant (red lines, after Arany et al. (2017)) foundations. Compliant-base predictions are extracted for each case from Table 6 to best-match PSD peak frequencies.

The PSD plots display the frequency content of all input/output signals over their whole duration, with peaks denoting the harmonics dominating the OWT response overall. It is immediately apparent in Figure 14 that the OWT response for $D_r$ = 60-80 % (i.e. relevant to the adopted monopile design) mostly spans a quite narrow frequency band, with peaks at frequencies bounded by the analytical $f_0$ predictions (fixed-base and compliant-base) in most instances. Conversely, the broad-band response visible in all $D_r$ = 40 % cases appears as a direct consequence of unsuitable foundation design and excessive soil non-linearity.

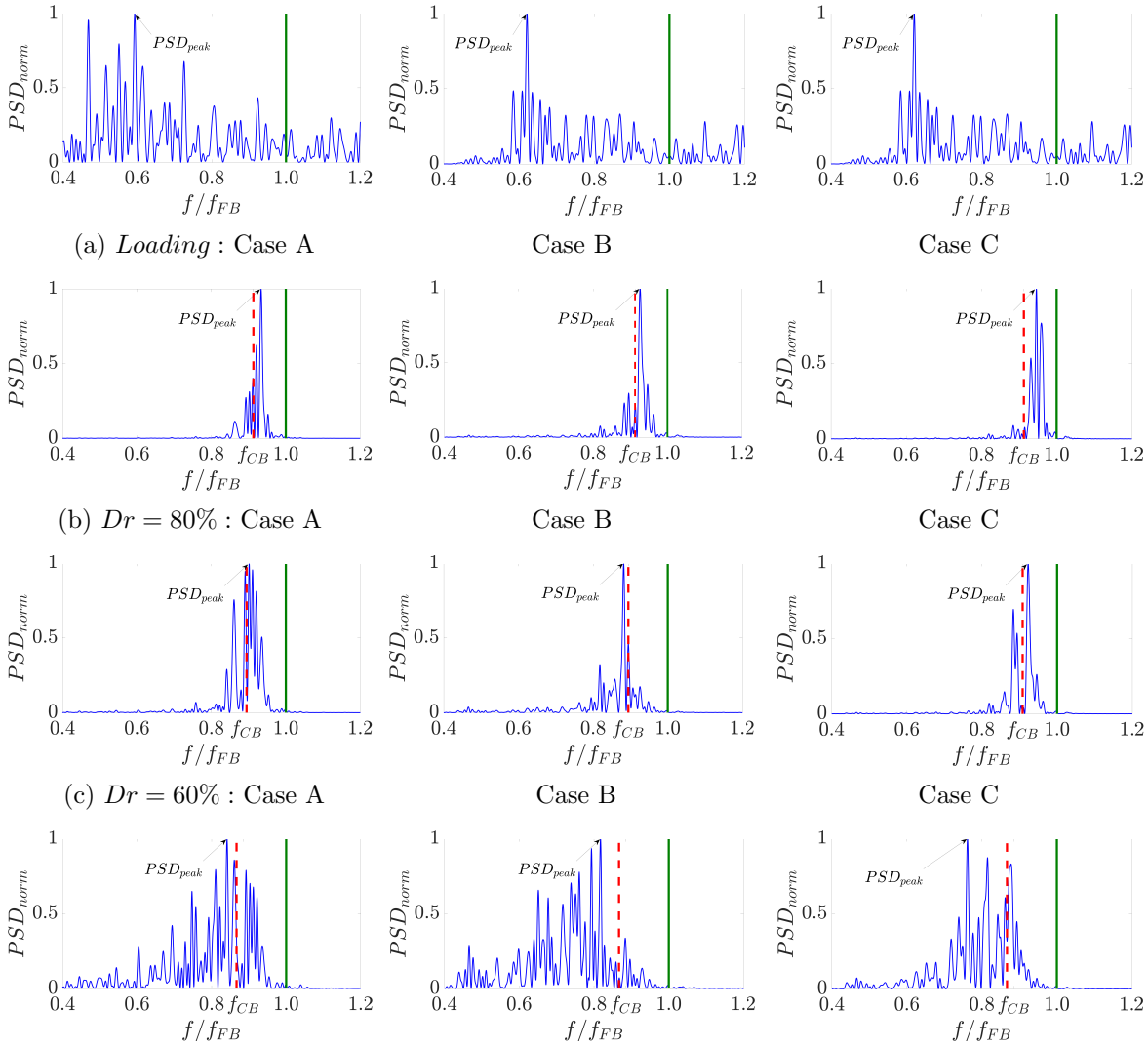


(a) *Loading* : Case A | Case B | Case C

(b) $Dr = 80\%$ : Case A | Case B | Case C

(c) $Dr = 60\%$ : Case A | Case B | Case C

(d) $Dr = 40\%$ : Case A | Case B | Case C

Figure 14: Normalised power spectral densities of (a) total lateral load histories and (b)-(d) OWT hub displacement. The vertical lines indicate analytical $f_0$ corresponding with fixed base (green, $f/f_{FB} = 1$) and compliant foundation (red-dashed, $f_{CB}$ – after Arany et al. (2017)).

### 5.2.2 Time-frequency analysis – Stockwell transforms

Following the interesting application in Kramer et al. (2016), time-frequency processing is exploited in this work as a tool to analyse the frequency response of OWTs as an evolving process. For this purpose, S(Stockwell)-transforms of input loading histories and OWT displacements are presented in Figures 15, 16 and 17 for Case A, Case B and Case C, respectively. The S-transform amplitudes are associated with the colourbars on the side and, for hub displacement transforms, normalised at each time with respect to the maximum value – this allows to track the peak frequency with the same yellow colour all along the time history. Fundamentals of S-transformation are summarised in Appendix A.2.

S-plots confirm altogether a strong dependence of the OWT response on $D_r$, as well as on the amplitude and frequency content of the input loading. When the OWT is founded on stiff/strong sand ($D_r = 80\%$), its response in the frequency domain exhibits a single main peak at the first eigenfrequency (compare to Figure 14), with only slight shifts in time; similar conclusions are fairly applicable to the $D_r = 60\%$ case as well. That is apparently not the case for $D_r = 40\%$, as witnessed by the very irregular evolution of the peak frequency (yellow band).

The abrupt changes in peak frequency for all $D_r = 40\%$ cases match the frequency content of the input excitation signal, and mark temporary transitions from 'resonance-dominated' to 'input-dominated' OWT response – compare e.g. for Case A (Figure 15) the frequency drops in the OWT response (Figure 15d) to the S-transform of the input load (Figure 15a) at times $t =$ 200, 300, 450 s. This undesired outcome of poor foundation design has not been found for higher $D_r$, and can be directly related to dynamic HM processes within the soil deposit. Table 5 points out the high soil damping in the $D_r = 40\%$ case: this may explain an OWT response compliant to (the frequency content of) the applied loads, with large foundation damping accelerating the dissipation of transient "eigen-motion" components at the global level.

It is interesting to observe in Figure 18 the pore pressure evolution at all previous control points. The inception of 'chaotic' frequency response for $D_r = 40\%$ correlates very well with the time $t \approx 300$ s at which the pore pressure ratio $u/p$ is beyond 0.9 at all control points. From that time onward the soil around the monopile can only mobilise very low stiffness due to reduced effective confinement, with an obvious effect on the global compliance of the foundation. The numerical results seem to confirm the conjecture of Kallehave et al. (2012): pore pressure effects may negatively impact OWT performance, especially in presence of under-designed foundations.

### 5.2.3 Comparison between analytical and numerical predictions

The S-plots in Figures 15–17 and the power density spectra in Figure 14 are also instrumental to compare analytical and numerical $f_0$ predictions. In particular, all S-plots include red dashed lines corresponding with best-fit analytical compliant-base predictions ($CB_{analytical}$).

Overall, the analytical relationships proposed by Gazetas (1984) seem to suit best the weak load scenario C, and thus loading conditions relevant to fatigue limit state. Good $f_0$ predictions can also be obtained through the formulas by Randolph (1981), regarded by Arany et al. (2017) as the most accurate along with those proposed by Poulos and Davis (1980). In the same work, Arany et al. also argued that formulations for flexible piles tend to produce better estimates of $f_0$, which is in full agreement with this study – compare values in Table 6 to Figures 14, 15, 16, 17.

As long as the foundation is properly designed (here for $D_r = 60$–$80\%$), the analytical predictions inspired by Arany et al. (2017) appear to provide solid lower bounds to the $f_0$ values resulting from 3D FE simulations.

## 5.3 Transient drops in natural frequency

Only a few literature studies investigated the dynamics of OWTs based on field monitoring and observations related to the geotechnical performance of the foundation. A notable example is the work by Kallehave et al. (2015b), in which the performance of a 2.3 MW OWT in dense to very dense sand is discussed after a monitoring period of 2.5 years. The OWT considered was founded on a monopile having length 18.4 m and diameter 3.9 m, and experienced only one strong storm during the monitoring period – see gray-shaded are in Figure 19a. The first natural frequency $f_0$ was estimated by post-processing acceleration signals recorded at the rotor-nacelle-assembly (RNA). Despite the differences in OWT size, soil conditions and environmental loads, it is still interesting to compare the $f_0$–drops recorded by Kallehave et al. (2015b) to the corresponding drops predicted in this study for an 8 MW wind turbine in stiff sand ($D_r = 80\%$). In particular, the experimental data associated with wind speeds of about 24 m/s and 47 m/s (see red and blue arrows in Figure 19a) are considered in the comparison.

The average $f_0$–drops for Case A and Case B have been derived from the S-plots in Figures 15–16, then associated with the average wind speeds underlying the thrust forces in Figure 3, respectively 24 m/s and 47 m/s. In both cases, the rotor was feathered, exactly as in Kallehave et al. (2015b) at the relevant time instants (red and blue arrows in Figure 19a). Figure 19b shows that the $f_0$–drops predicted in this study for an 8 MW OWT compare very well to the measured values reported by Kallehave et al. (2015b), with simulated $f_0$–drops never below 3% of the original value.

It may be concluded that transient drops in natural frequency do not appear as serious hazard when current design practice is correctly implemented. If that is the case – like in this study for $D_r = 80\%$ – soil non-linearity does not affect dramatically the OWT frequency response, not even under severe storm loading. The encouraging comparison between field data and numerical predictions also adds confidence about the use of advanced 3D FE analyses for design purposes.

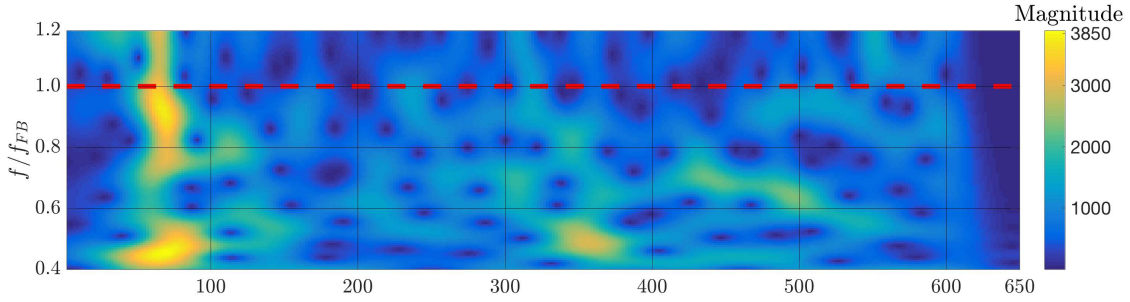


(a) Load A

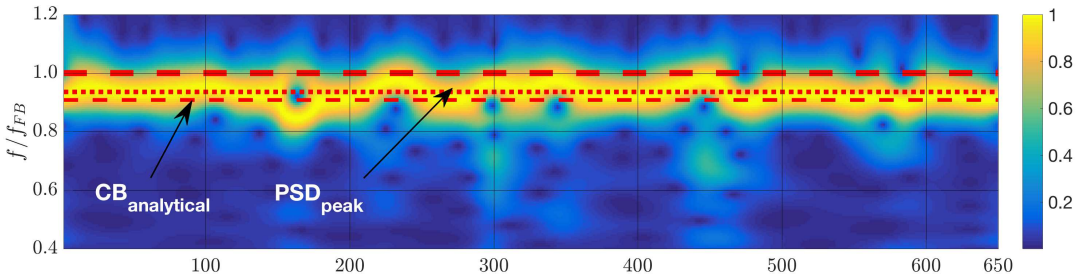


(b) $Dr = 80\%,\ PSD_{peak} = 0.931\ f/f_{FB},\ CB_{analytical} = 0.913\ f/f_{FB}$ based on Gazetas (1984)

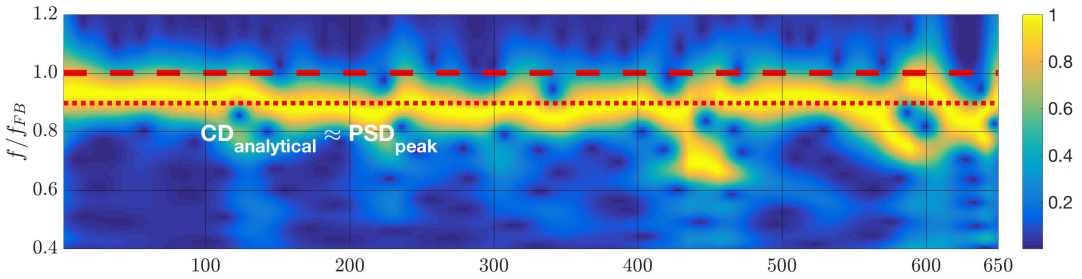


(c) $Dr = 60\%,\ PSD_{peak} = 0.899\ f/f_{FB},\ CB_{analytical} = 0.895\ f/f_{FB}$ based on Randolph (1981)

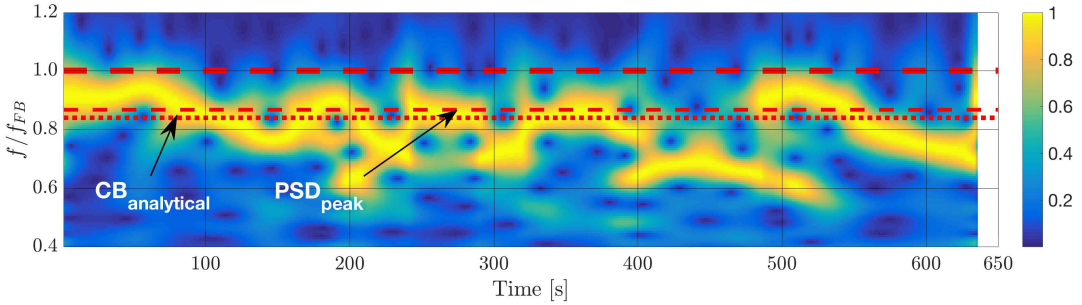


(d) $Dr = 40\%,\ PSD_{peak} = 0.840\ f/f_{FB},\ CB_{analytical} = 0.867\ f/f_{FB}$ based on Shadlou and Bhattacharya (2016)

Figure 15: S-plots for Case A: (a) input load (non-normalised and (b)-(d) hub displacement for $D_r = 80\%, 60\%, 40\%$. Fixed-base $f_0/f_{FB} = 1$. $PSD_{peak}$ denotes the peak frequency in the corresponding $PSD_{norm}$ plot in Figure 14. Colourbars indicate the amplitude of harmonics within the range (0.4–1.2) $\times$ $f_0/f_{FB}$.

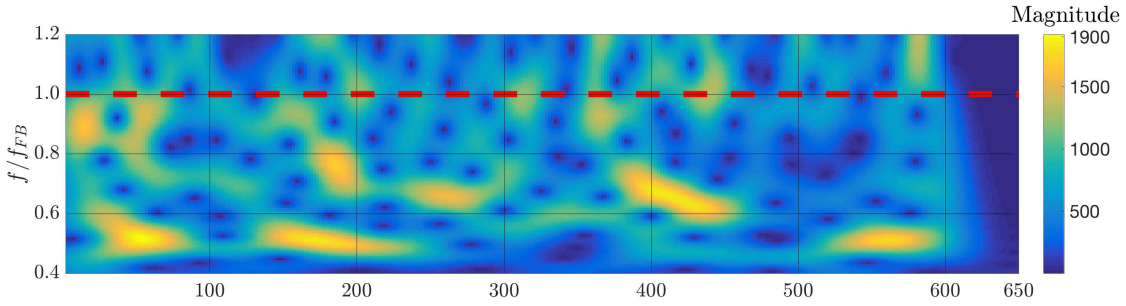


(a) Load B

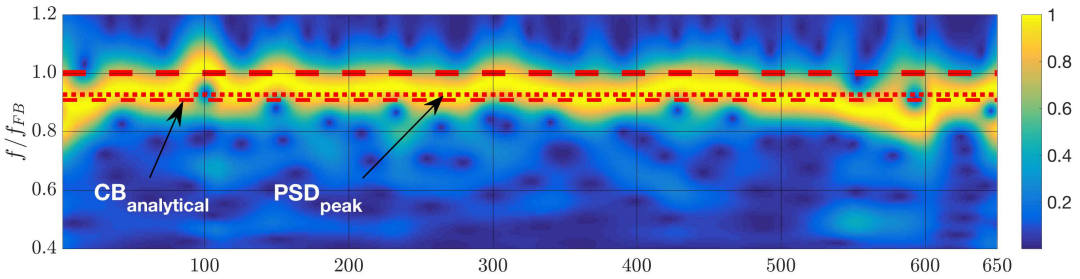


(b) $Dr = 80\%,\ PSD_{peak} = 0.927\ f/f_{FB},\ CB_{analytical} = 0.913\ f/f_{FB}$ Hz based on Gazetas (1984)

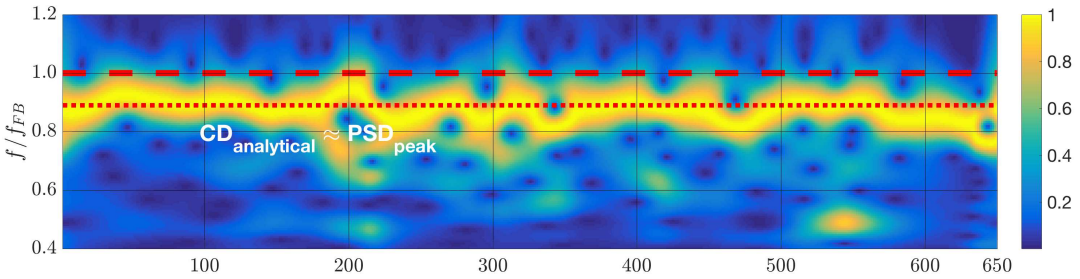


(c) $Dr = 60\%,\ PSD_{peak} = 0.881\ f/f_{FB},\ CB_{analytical} = 0.895\ f/f_{FB}$ based on Randolph (1981)

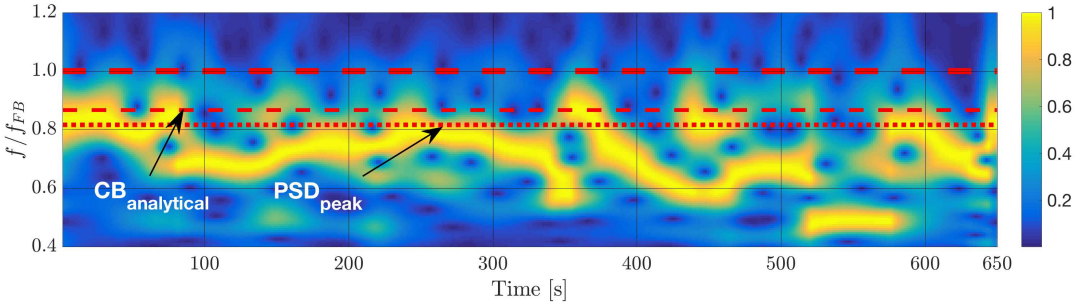


(d) $Dr = 40\%,\ PSD_{peak} = 0.817\ f/f_{FB},\ CB_{analytical} = 0.867\ f/f_{FB}$ based on Shadlou and Bhattacharya (2016)

Figure 16: S-plots for Case B: (a) input load (non-normalised and (b)-(d) hub displacement for $D_r = 80\%, 60\%, 40\%$. Fixed-base $f_0/f_{FB} = 1$. $PSD_{peak}$ denotes the peak frequency in the corresponding $PSD_{norm}$ plot in Figure 14. Colourbars indicate the amplitude of harmonics within the range $(0.4\text{–}1.2) \times f_0/f_{FB}$.

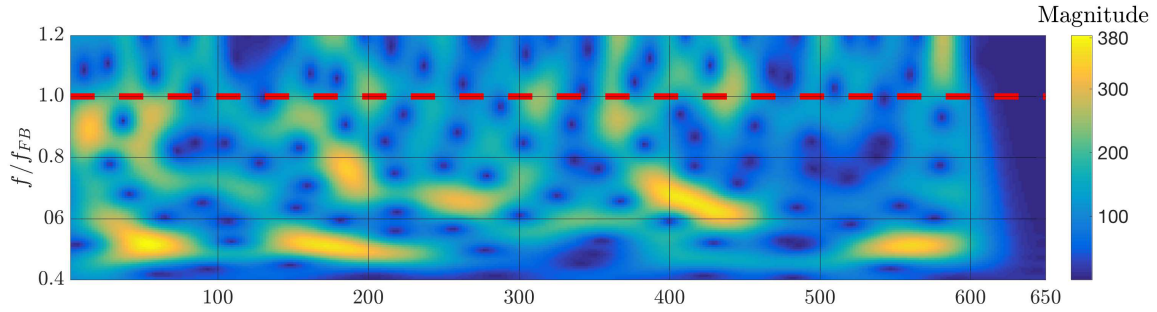


(a) Load C

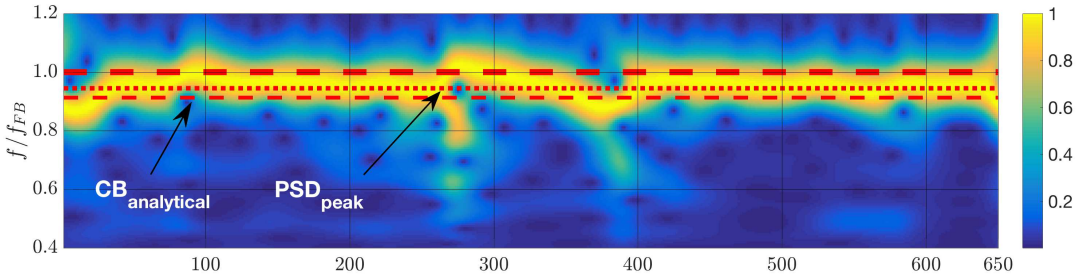


(b) $Dr = 80\%$, $PSD_{peak} = 0.945\ f/f_{FB}$, $CB_{analytical} = 0.913\ f/f_{FB}$ based on Gazetas (1984)

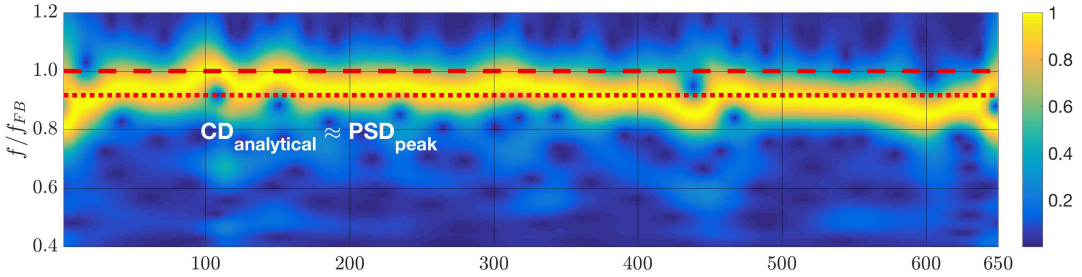


(c) $Dr = 60\%$, $PSD_{peak} = 0.922\ f/f_{FB}$, $CB_{analytical} = 0.908\ f/f_{FB}$ based on Gazetas (1984)

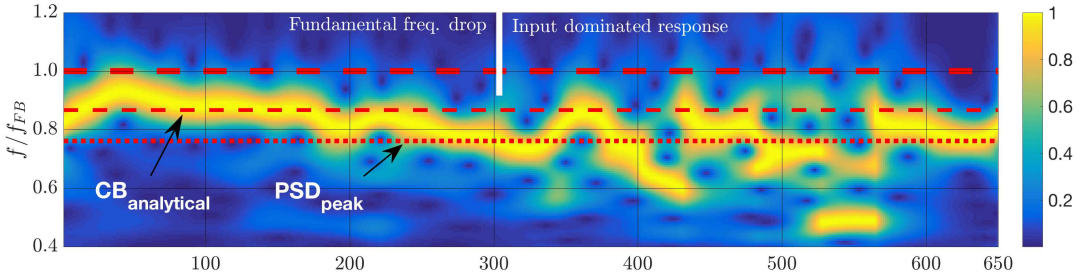


(d) $Dr = 40\%$, $PSD_{peak} = 0.762\ f/f_{FB}$, $CB_{analytical} = 0.867\ f/f_{FB}$ based on Shadlou and Bhattacharya (2016)

Figure 17: S-plots for Case C: (a) input load (non-normalised and (b)-(d) hub displacement for $D_r = 80\%$, 60%, 40%. Fixed-base $f_0/f_{FB} = 1$. $PSD_{peak}$ denotes the peak frequency in the corresponding $PSD_{norm}$ plot in Figure 14. Colourbars indicate the amplitude of harmonics within the range (0.4–1.2) $\times$ $f_0/f_{FB}$.

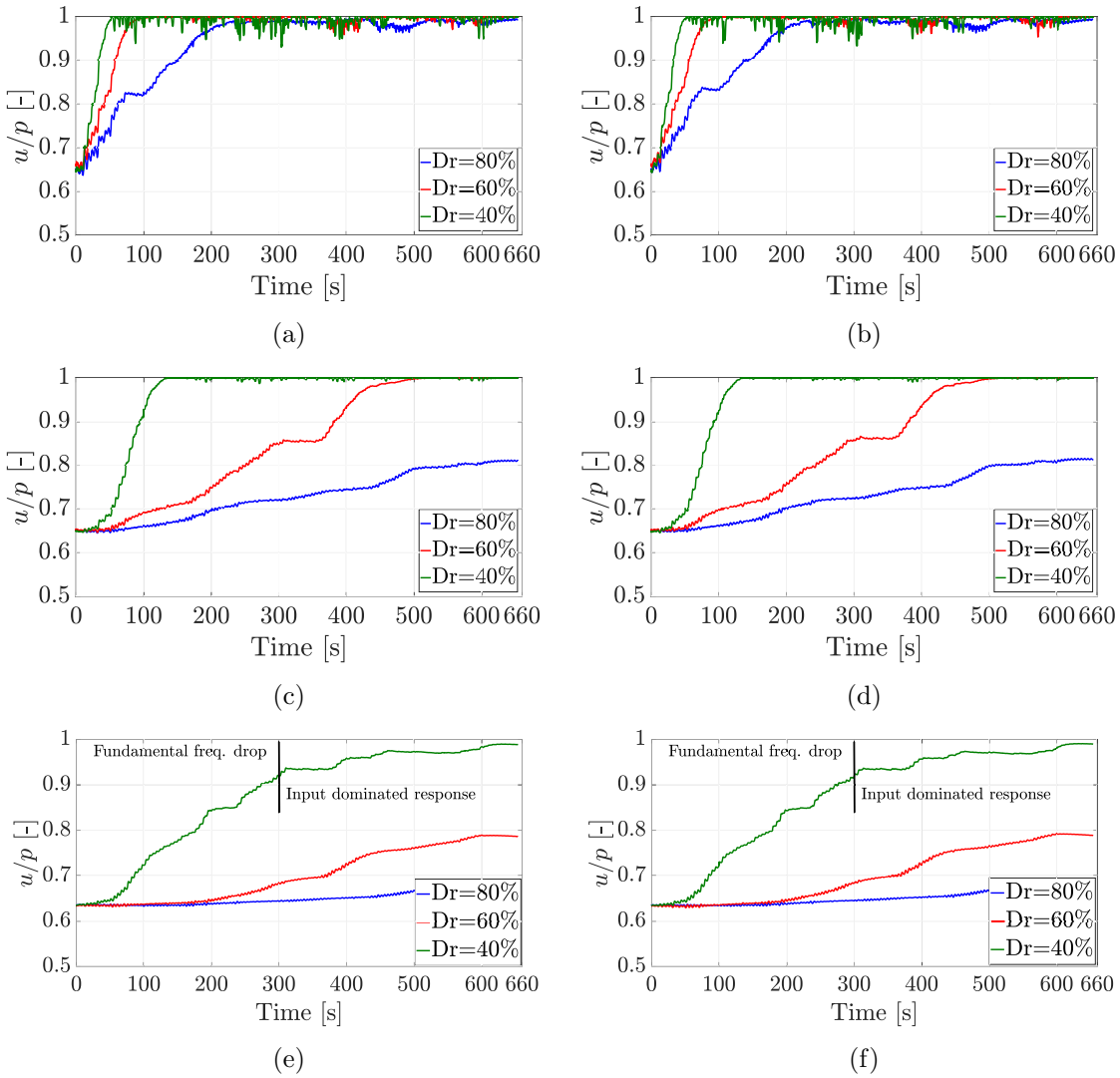


Figure 18: Time evolution of the pore pressure ratio $u/p$ at all control points for Case C: (a) $A_L$, (b) $A_R$, (c) $B_L$, (d) $B_R$, (e) $C_L$, (f) $C_R$.

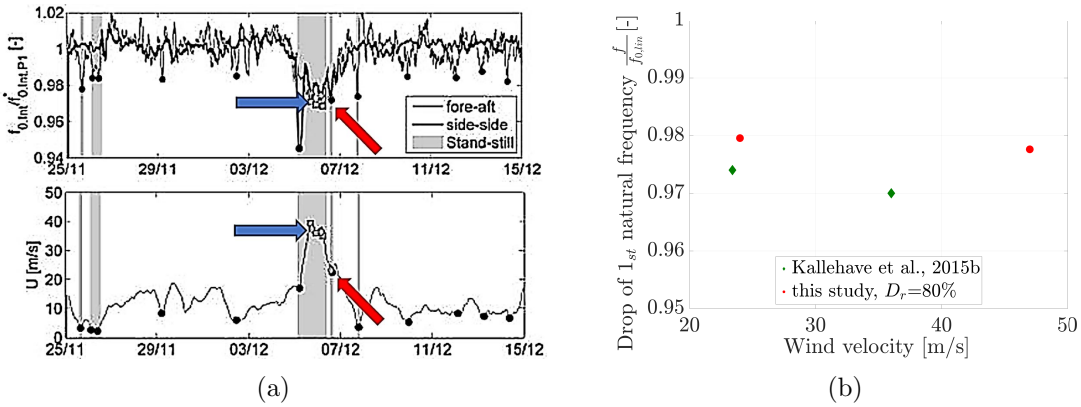


Figure 19: (a) Field measurements on a 2.3 MW OWT (adapted after Kallehave et al. (2015b)). Top: time-evolution of $f_0$ for fore-aft and side-side vibrations under normal operations. Bottom: wind speed (grey areas denote feathered rotors); (b) $f_0$–drops vs wind speed for parked OWTs, after Kallehave et al. (2015b) and this study (8MW OWT) – $f_0$ normalised with respect to its linear/weak-vibration value $f_{0,lin}$.

# 6 Concluding Remarks

An integrated 3D FE model was set up to investigate the dynamic response of OWT-monopile-sand systems to severe storm events, with emphasis on global OWT damping and transient drops in natural frequency. Relevant features of the FE model are:

- state-of-practice structural configuration, representative of an 8 MW OWT supported by a large-diameter monopile;
- dynamic simulation of soil-foundation interaction accounting for pore pressure build-up and dissipation ($u - p$ dynamic formulation);
- hydro-mechanical plasticity modelling of cyclic sand behaviour based on the SANISAND04 critical state formulation;
- realistic scenarios of environmental loading (wind and waves), long-duration dynamic analyses (duration: 10 minutes).

Sandy soil conditions were considered for three initial relative densities. The numerical results showed good agreement with previous lessons learned from field tests and industry projects. 3D FE simulations enabled to explore interesting hydro-mechanical effects related to soil non-linearity, mostly impenetrable for traditional design methods. The following main conclusions were drawn:

- in presence of sound monopile design in sand, transient drops in OWT natural frequency in the order of 2-3% should be expected, even in response to strong storms. However, further optimisation of monopile design may alter this conclusion;
- analytical approaches for the estimation of the first OWT natural frequency, e.g. Arany et al. (2017), proved in conservative agreement with 3D FE results for $D_r = 80\%$–$60\%$, and which in turn emphasised the relevance of soil-monopile interaction during small vibrations. Even under extreme environmental conditions, the current design practice in sandy soils appears robust/safe with respect to transient shifts in natural frequency;
- partial water drainage around the monopile can impact the global OWT damping, more pronouncedly during weak vibrations. This aspect suggests that fully drained or undrained analyses may miss important aspects of the global behaviour, so far not documented in the literature;
- inappropriate monopile (under-)design can dangerously shift the OWT response towards lower frequencies – see $D_r = 40\%$ case. Severe seabed scour is also envisaged to possibly cause similar effects.

This work opened to closer integration between advanced geotechnical analysis and simplified engineering methods, while re-questioning the validity of design approaches not derived from rigorous 3D principles – the case of old p-y formulations for slender piles is particularly emblematic in this respect.

Nonetheless, even at the current state of the art, advanced modelling must be handled with care in its application to design. Further research is needed to improve (i) simulation of soil cyclic behaviour, (ii) calibration of soil parameters against in-situ and laboratory test results, (iii) computational performance through parallel computing.

# Acknowledgements

Siemens Gamesa Renewable Energy (The Hague, The Netherlands) is gratefully acknowledged for sharing OWT design details. In particular, the valuable inputs of Axel Nernheim and Vasilis Michalopoulos on geotechnical aspects and load modelling are especially appreciated.

## References

Achmus, M., Kuo, Y.-S., and Abdel-Rahman, K. (2009). Behavior of monopile foundations under cyclic lateral load. *Computers and Geotechnics*, 36(5):725–735.

Arany, L., Bhattacharya, S., Adhikari, S., Hogan, S., and McDonald, J. (2015). An analytical model to predict the natural frequency of offshore wind turbines on three-spring flexible foundations using two different beam models. *Soil Dynamics and Earthquake Engineering*, 74:40–45.

Arany, L., Bhattacharya, S., Macdonald, J., and Hogan, S. (2017). Design of monopiles for offshore wind turbines in 10 steps. *Soil Dynamics and Earthquake Engineering*, 92:126–152.

Arany, L., Bhattacharya, S., Macdonald, J. H., and Hogan, S. J. (2016). Closed form solution of eigen frequency of monopile supported offshore wind turbines in deeper waters incorporating stiffness of substructure and ssi. *Soil Dynamics and Earthquake Engineering*, 83:18–32.

Balog, I., Ruti, P. M., Tobin, I., Armenio, V., and Vautard, R. (2016). A numerical approach for planning offshore wind farms from regional to local scales over the Mediterranean. *Renewable Energy*, 85:395–405.

Barari, A., Bagheri, M., Rouainia, M., and Ibsen, L. B. (2017). Deformation mechanisms for offshore monopile foundations accounting for cyclic mobility effects. *Soil Dynamics and Earthquake Engineering*, 97:439–453.

Been, K. and Jefferies, M. (1985). A state parameter for sands. *Géotechnique*, 35(2):99–112.

Bhattacharya, S., Cox, J. A., Lombardi, D., and Wood, D. M. (2013). Dynamics of offshore wind turbines supported on two foundations. *Proceedings of the Institution of Civil Engineers: Geotechnical Engineering*, 166:159–169.

BS EN (1991). 1-4: 2005 eurocode 1: Actions on structures - general actions - wind actions.

Byrne, B., McAdam, R., Burd, H., Houlsby, G., Martin, C., Beuckelaers, W., Zdravkovic, L., Taborа, D., Potts, D., Jardine, R., Ushev, E., Liu, T., Abadias, D., Gavin, K., Igoe, D., Doherty, P., Skov Gretlund, J., Pacheco Andeade, M., Muir Wood, A., Schroeder, F., Turner, S., and Plummer, M. (2017). Pisa: New design methods for offshore wind tutbine monopiles. In *Offshore Site Investigation and Geotechnics: Smarter Solutions for Future Offshore Developments*. Society of Underwater Technology.

Carswell, W., Johansson, J., Løvholt, F., Arwade, S. R., and DeGroot, D. J. (2014). Dynamic mudline damping for offshore wind turbine monopiles. In *Proceedings of the ASME 2014 33rd international conference on ocean, offshore and arctic engineering OMAE2014 June*, volume 8, page 13.

Christoforaki, M. and Tsoutsos, T. (2017). Sustainable siting of an offshore wind park a case in Chania, Crete. *Renewable Energy*, 109:624–633.

Corciulo, S. (2016). Dynamic hydro-mechanical analysis of soil-monopile interaction in offshore wind turbines. Master's thesis, Politecnico di Milano, Italy.

Corciulo, S., Zanoli, O., and Pisanò, F. (2017a). Supporting the engineering analysis of offshore wind turbines through advanced soil-structure 3D modelling. In *ASME 2017 36th International Conference on Ocean, Offshore and Arctic Engineering*, pages V009T10A015–V009T10A015. American Society of Mechanical Engineers.

Corciulo, S., Zanoli, O., and Pisanò, F. (2017b). Transient response of offshore wind turbines on monopiles in sand: role of cyclic hydro–mechanical soil behaviour. *Computers and Geotechnics*, 83:221–238.

Cuéllar, P., Mira, P., Pastor, M., Fernández-Merodo, J. A., Baeßler, M., and Rücker, W. (2014). A numerical model for the transient analysis of offshore foundations under cyclic loading. *Computers and Geotechnics*, 59:75–86.

Dafalias, Y. and Taiebat, M. (2016). SANISAND-Z: zero elastic range sand plasticity model. *Géotechnique*, 66(12):999–1013.

Dafalias, Y. F. and Manzari, M. T. (2004). Simple plasticity sand model accounting for fabric change effects. *Journal of Engineering mechanics*, 130(6):622–634.

Damgaard, M., Andersen, J., Ibsen, L., and Andersen, L. (2013). Time-varying dynamic properties of offshore wind turbines evaluated by modal testing. In *18th International Conference on Soil Mechanics and Geotechnical Engineering (ICSMGE2013)*. International Society of Soil Mechanics and Geotechnical Engineering (ISSMGE).

Damgaard, M., Andersen, J. K., et al. (2012). Natural frequency and damping estimation of an offshore wind turbine structure. In *The Twenty-second International Offshore and Polar Engineering Conference*. International Society of Offshore and Polar Engineers.

Devriendt, C., Jordaens, P. J., De Sitter, G., and Guillaume, P. (2013). Damping estimation of an offshore wind turbine on a monopile foundation. *IET Renewable Power Generation*, 7(4):401–412.

DNV (2014). DNV-OS-J101 offshore standard: Design of offshore wind turbine structures. *DNV AS, Høvik, Norway*.

Doherty, P. and Gavin, K. (2012). Laterally loaded monopile design for offshore wind farms. *Proceedings of the Institution of Civil Engineers - Energy*, 165(1):7–17.

Gajo, A. (1995). Influence of viscous coupling in propagation of elastic waves in saturated soil. *Journal of geotechnical engineering*, 121(9):636–644.

Gazetas, G. (1984). Seismic response of end-bearing single piles. *International Journal of Soil Dynamics and Earthquake Engineering*, 3(2):82–93.

Germanische Lloyd (2005). Guideline for the Certification of Offshore Wind Turbines.

Ghofrani, A. and Arduino, P. (2017). Prediction of LEAP centrifuge test results using a pressure-dependent bounding surface constitutive model. *Soil Dynamics and Earthquake Engineering*.

Griffiths, D. V. (1985). Numerical modeling of interfaces using conventional finite elements. In *Proceedings of 5th International Conference on Numerical Methods in Geomechanics. Nagoya, Japan*, pages 837–844.

He, Y., Byrne, B., and Burd, H. (2017). Application of a numerical-based design method for laterally loaded monopiles in layered soils. In *Offshore Site Investigation and Geotechnics: Smarter Solutions for Future Offshore Developments*. Society of Underwater Technology.

Huang, M., Yue, Z. Q., Tham, L. G., and Zienkiewicz, O. C. (2004). On the stable finite element procedures for dynamic problems of saturated porous media. *International Journal for Numerical Methods in Engineering*, 61(9):1421–1450.

Hughes, T. J. R. (1987). *The Finite Element Method: linear static and dynamic finite element analysis*. Prentice-Hall.

Jeremić, B., Cheng, Z., Taiebat, M., and Dafalias, Y. F. (2008). Numerical simulation of fully saturated porous materials. *International Journal for Numerical and Analytical Methods in Geomechanics*, 32(13):1635–1660.

Kallehave, D., Byrne, B. W., Thilsted, C. L., and Mikkelsen, K. K. (2015a). Optimization of monopiles for offshore wind turbines. *Philosophical Transactions of the Royal Society of London A: Mathematical, Physical and Engineering Sciences*, 373(2035):1–15.

Kallehave, D., Thilsted, C., and Diaz, A. T. (2015b). Observed variations of monopile foundation stiffness. In *The 3rd Internationl symposium on Frontiers in offshore Geotechnics*, pages 717–722. CRC Press LLC.

Kallehave, D., Thilsted, C. L., and Liingaard, M. (2012). Modification of the API p-y formulation of initial stiffness of sand. In *Proceedings of Offshore Site Investigation and Geotechnics: Integrated Technologies - Present and Future. London, UK*, pages 465–472. Society of Underwater Technology.

Kementzetzidis, E. (2017). Geotechnical aspects of offshore wind turbine dynamics emerging from 3D sand-monopile non-linear simulations. Master's thesis, Delft University of Technology, The Netherlands.

Kementzetzidis, E., Versteijlen, W. G., Nernheim, A., and Pisanò, F. (2018). 3d fe dynamic modelling of offshore wind turbines in sand: natural frequency evolution in the pre– to after-storm transition. In *In Proceedings of the 9th European conference on Numerical Methods in Geotechnical Engineering (NUMGE 2018), Porto, Portugal*.

Kramer, S., Sideras, S., and Greenfield, M. (2016). The timing of liquefaction and its utility in liquefaction hazard evaluation. *Soil Dynamics and Earthquake Engineering*, 91:133–146.

LeBlanc, C., Houlsby, G. T., and Byrne, B. W. (2010). Response of stiff piles in sand to long-term cyclic lateral loading. *Géotechnique*, 60(2):79–90.

Leblanc, C. and Tarp-Johansen, N. J. (2010). Monopiles in sand. stiffness and damping.

Liu, H., Abell, J. A., Diambra, A., and Pisanò, F. (2018a). Modelling the cyclic ratcheting of sands through memory-enhanced bounding surface plasticity. *Géotechnique*, accepted for publication.

Liu, H., Zygounas, F., Diambra, A., and Pisanò, F. (2018b). Enhanced plasticity modelling of high-cyclic ratcheting and pore pressure accumulation in sands. In *In Proceedings of the 9th European conference on Numerical Methods in Geotechnical Engineering (NUMGE 2018), Porto, Portugal*.

López-Querol, S., Fernández-Merodo, J. A., Mira, P., and Pastor, M. (2008). Numerical modelling of dynamic consolidation on granular soils. *International journal for numerical and analytical methods in geomechanics*, 32(12):1431–1457.

Manzari, M. T. and Dafalias, Y. F. (1997). A critical state two-surface plasticity model for sands. *Géotechnique*, 47(2):255–272.

Mazzoni, S., McKenna, F., Scott, M., and Fenves, G. (2007). *OpenSees Command Language Manual*.

McGann, C. R., Arduino, P., and Mackenzie-Helnwein, P. (2015). A stabilized single-point finite element formulation for three-dimensional dynamic analysis of saturated soils. *Computers and Geotechnics*, 66:126–141.

McKenna, F. T. (1997). *Object-oriented finite element programming: frameworks for analysis, algorithms and parallel computing*. PhD thesis, University of California, Berkeley.

Newman, J. N. (1977). *Marine hydrodynamics*. MIT press.

Papadimitriou, A. G. and Bouckovalas, G. D. (2002). Plasticity model for sand under small and large cyclic strains: a multiaxial formulation. *Soil Dynamics and Earthquake Engineering*, 22(3):191–204.

Papadimitriou, A. G., Bouckovalas, G. D., and Dafalias, Y. F. (2001). Plasticity model for sand under small and large cyclic strains. *Journal of Geotechnical and Geoenvironmental Engineering*, 127(11):973–983.

Pisanò, F. and Gavin, K. G. (2017). General report for TC209 - Offshore Geotechnics. In *19th International Conference on Soil Mechanics and Geotechnical Engineering (ICSMGE2017)*. International Society of Soil Mechanics and Geotechnical Engineering (ISSMGE).

Pisanò, F. and Jeremić, B. (2014). Simulating stiffness degradation and damping in soils via a simple visco-elastic–plastic model. *Soil Dynamics and Earthquake Engineering*, 63:98–109.

Poulos, H. G. and Davis, E. H. (1980). *Pile foundation analysis and design*. Number Monograph.

Prendergast, L. J. and Gavin, K. (2016). A comparison of initial stiffness formulations for small-strain soil–pile dynamic winkler modelling. *Soil Dynamics and Earthquake Engineering*, 81:27–41.

Ramirez, J., Barrero, A. R., Chen, L., Dashti, S., Ghofrani, A., Taiebat, M., and Arduino, P. (2018). Site response in a layered liquefiable deposit: evaluation of different numerical tools and methodologies with centrifuge experimental results. *Journal of Geotechnical and Geoenvironmental Engineering*, 144(10):04018073.

Randolph, M. F. (1981). The response of flexible piles to lateral loading. *Géotechnique*, 31(2):247–259.

Randolph, M. F. and Gourvenec, S. (2011). *Offshore Geotechnical Engineering*. Spon Press.

Schanz, M. (2009). Poroelastodynamics: linear models, analytical solutions, and numerical methods. *Applied mechanics reviews*, 62(3):030803.

Schweizer, J., Antonini, A., Govoni, L., Gottardi, G., Archetti, R., Supino, E., Berretta, C., Casadei, C., and Ozzi, C. (2016). Investigating the potential and feasibility of an offshore wind farm in the Northern Adriatic Sea. *Applied Energy*, 177:449–463.

Senanayake, A., Gilbert, R. B., and Manuel, L. (2017). Estimating natural frequencies of monopile supported offshore wind turbines using alternative p-y models. In *Offshore Technology Conference*. Offshore Technology Conference.

Shadlou, M. and Bhattacharya, S. (2016). Dynamic stiffness of monopiles supporting offshore wind turbine generators. *Soil Dynamics and Earthquake Engineering*, 88:15–32.

Shirzadeh, R., Devriendt, C., Bidakhvidi, M. A., and Guillaume, P. (2013). Experimental and computational damping estimation of an offshore wind turbine on a monopile foundation. *Journal of Wind Engineering and Industrial Aerodynamics*, 120:96–106.

Sloan, S. W. (1987). Substepping schemes for the numerical integration of elastoplastic stress–strain relations. *International Journal for Numerical Methods in Engineering*, 24(5):893–911.

Stockwell, R. G., Mansinha, L., and Lowe, R. (1996). Localization of the complex spectrum: the s transform. *IEEE transactions on signal processing*, 44(4):998–1001.

Taiebat, M. and Dafalias, Y. F. (2008). SANISAND: Simple anisotropic sand plasticity model. *International Journal for Numerical and Analytical Methods in Geomechanics*, 32(8):915–948.

Taiebat, M., Jeremić, B., Dafalias, Y. F., Kaynia, A. M., and Cheng, Z. (2010). Propagation of seismic waves through liquefied soils. *Soil Dynamics and Earthquake Engineering*, 30(4):236–257.

Tarp-Johansen, N. J., Andersen, L., Christensen, E. D., Mørch, C., Frandsen, S., and Kallesøe, B. (2009). Comparing sources of damping of cross-wind motion. In *The European Offshore Wind Conference & Exhibition*. The European Wind Energy Association.

van Kuik, G. A. M., Peinke, J., Nijssen, R., Lekou, D. J., Mann, J., Sørensen, J. N., Ferreira, C., van Wingerden, J. W., Schlipf, D., Gebraad, P., et al. (2016). Long-term research challenges in wind energy–a research agenda by the European Academy of Wind Energy. *Wind Energy Science*, 1:1–39.

Verdugo, R. and Ishihara, K. (1996). The steady state of sandy soils. *Soils and foundations*, 36(2):81–91.

Versteijlen, W., De Vries, W., Metrikine, A., Hoving, J., and Smidt, E. (2011). Estimation of the vibration decrement of an offshore wind turbine support structure caused by its interaction with soil. In *Proceedings of the EWEA Offshore 2011 Conference, Amsterdam, The Netherlands, 29 November-1 December 2011*. European Wind Energy Association.

Versteijlen, W., Renting, F., van der Valk, P., Bongers, J., van Dalen, K., and Metrikine, A. (2017). Effective soil-stiffness validation: shaker excitation of an in-situ monopile foundation. *Soil Dynamics and Earthquake Engineering*, 102:241 – 262.

Versteijlen, W. G., Metrikine, A. V., and van Dalen, K. N. (2016). A method for identification of an effective Winkler foundation for large-diameter offshore wind turbine support structures based on in-situ measured small-strain soil response and 3D modelling. *Engineering Structures*, 124:221–236.

Wood, D. M., Belkheir, K., and Liu, D. F. (1994). Strain softening and state parameter for sand modelling. *Géotechnique*, 44(2):335–339.

Zdravković, L., Taborda, D., Potts, D., Jardine, R., Sideri, M., Schroeder, F., Byrne, B., McAdam, R., Burd, H., Houlsby, G., et al. (2015). Numerical modelling of large diameter piles under lateral loading for offshore wind applications. In *Proceeding 3rd International Symposium on Frontiers in Offshore Geotechnics. Norway:[sn]*.

Zienkiewicz, O. C., Chang, C. T., and Bettess, P. (1980). Drained, undrained, consolidating and dynamic behaviour assumptions in soils. *Géotechnique*, 30(4):385–395.

Zienkiewicz, O. C. and Shiomi, T. (1984). Dynamic behaviour of saturated porous media; the generalized Biot formulation and its numerical solution. *International Journal for Numerical and Analytical Methods in Geomechanics*, 8(1):71–96.

Zountouridou, E., Kiokes, G., Chakalis, S., Georgilakis, P., and Hatziargyriou, N. (2015). Offshore floating wind parks in the deep waters of Mediterranean Sea. *Renewable and Sustainable Energy Reviews*, 51:433–448.

# A Appendix

## A.1 Analytical determination of $f_0$ according to Arany et al. (2017)

The analytical procedure by Arany et al. (2017) for determining the OWT natural frequency $f_0$ is summarised in this appendix. The procedure is based on the following representation of $f_0$:

$$f_0 = C_L C_R C_S f_{FB} \tag{2}$$

where $f_{FB}$ is the natural frequency of the same OWT with a clamped/fixed base, $C_L$ and $C_R$ account for the lateral and rotational flexibility of the foundation, and $C_S$ for the flexibility of the substructure. The elastic component $C_S f_{FB}$ was directly obtained from the FE OWT model, and included the flexibility of all structural members above the mudline.

Foundation compliances were instead calculated analytically according to Shadlou and Bhattacharya (2016):

$$C_R = 1 - \frac{1}{1 + \alpha\left(\eta_R - \frac{\eta_{LR}^2}{\eta_L}\right)} \qquad C_L = 1 - \frac{1}{1 + b\left(\eta_L - \frac{\eta_{LR}^2}{\eta_R}\right)} \tag{3}$$

where

$$\eta_L = \frac{K_L L_T^3}{EI_\eta} \qquad \eta_{LR} = \frac{K_{LR} L_T^2}{EI_\eta} \qquad \eta_R = \frac{K_R L_T}{EI_\eta} \tag{4}$$

$K_L$, $K_R$, $K_{LR}$ are foundation stiffness factors indicated by Shadlou and Bhattacharya (2016), $L_T$ and $EI_\eta$ the length and the equivalent bending stiffness of the tower. In particular:

$$EI_\eta = E_T I_T f(q) = E_T I_T \left[\frac{1}{3}\frac{2q^2(q-1)^3}{2q^2 \ln q - 3q^2 + 4q - 1}\right] \tag{5}$$

in which $q = D_b/D_t$ is the ratio between the structure diameters at the base ($D_b$) and at the top ($D_t$). The above foundation stiffness factors are evaluated for a monopile in homogeneous soil as follows (Shadlou and Bhattacharya, 2016):

$$K_L = \frac{1.45 E_{S0} D_p}{f_{vs}}\left(\frac{E_{eq}}{E_{S0}}\right)^{0.186} \qquad K_{LR} = -\frac{0.3 E_{S0} D_p^2}{f_{vs}}\left(\frac{E_{eq}}{E_{S0}}\right)^{0.5} \qquad K_R = \frac{0.18 E_{S0} D_p^3}{f_{vs}}\left(\frac{E_{eq}}{E_{S0}}\right)^{0.73} \tag{6}$$

$$E_{eq} = \frac{64 E_p I_p}{\pi D_p^4} \tag{7}$$

where $L_p$, $D_p$ and $I_p$ are the length, diameter and cross-sectional moment of inertia of the monopile. $f_{vs} = 1 + |\nu - 0.25|$ accounts for the soil Poisson's ratio $\nu$, while $E_{S0}$ denotes the (small-strain) Young modulus of the soil at the depth of one monopile diameter ($z = D_p$). For the FE model developed in this study, $E_{S0}$ was readily obtained from SANISAND04 constitutive equations (Dafalias and Manzari, 2004):

$$G(e,p) = G_0 p_{atm} \frac{(2.97 - e_0)^2}{1 + e_0}\left(\frac{p_0'}{p_{atm}}\right)^{0.5} \Rightarrow E_{S0} = 2(1+\nu) G(e_0, p_{0,z=D_p}) \tag{8}$$

in which $p_{atm}$ is the atmospheric pressure, $G_0$ a dimensionless small-strain stiffness parameter, $e_0$ and $p_0'$ the void ratio and the mean effective stress at $z = D_p$ after gravity loading.

## A.2 S(Stockwell)-transform

The time-frequency analysis of the OWT response in Section 5 was carried out through so-called S(Stockwell)-transformation. This allowed to capture transient shifts in natural frequency $f_0$, and in general to identify dominant harmonics in structural vibrations at elapsing time.

The S-transform was originally introduced as an extension of continuous wavelet transformation, with respect to which the former offers enhanced frequency resolution (Stockwell et al., 1996). This is achieved by applying a time-shifting frequency-dependent Gaussian window $w(t-\tau, f)$ to the Fourier transform of the signal $u(t)$ under consideration:

$$S(\tau, f) = \int_{-\infty}^{\infty} u(t) w(t-\tau, f) e^{-2i\pi f t} dt \tag{9}$$

where

$$w(t, f) = \frac{|f|}{k_S\sqrt{2\pi}} e^{-\frac{f^2 t^2}{2k_S^2}} \tag{10}$$

and $f$, $t$ and $\tau$ stand for frequency, time, and moving centre of the Gaussian window, respectively. The scalar parameter $k_S$ in Equation (10) is a positive scaling factor governing the window width. Large $k_S$ values produce high resolution in frequency but not in time. After a careful sensitivity analysis, $k_S = 0.2$ has been used throughout this study to compromise on time and frequency resolutions.